How orcas capture seals resting on ice floes

Original
How orcas capture seals resting on ice floes / Zhou, Wenyuan; An, Jiale; Rondoni, Lamberto; Zhang, Yuliang; Ou, Zhaoyang; He, Yang; Yuan, Weizheng. - In: JOURNAL OF FLUID MECHANICS. - ISSN 0022-1120. - ELETTRONICO. - 1034:(2026), pp. 1-51. [10.1017/jfm.2026.11483]

Publisher:
Cambridge University Press

Published
DOI:10.1017/jfm.2026.11483

Under consideration for publication in J. Fluid Mech.

How killer whales capture seals resting on ice floes

Wenyuan Zhou[1,2,3,4], Jiale An[5], Lamberto Rondoni[4], Yuliang Zhang[1,2,3], Zhaoyang Ou[1,2,3], Yang He[1,2,3] and Weizheng Yuan[1,2,3]

[1]Key Laboratory of Micro/Nano Systems for Aerospace, Ministry of Education, 710072 Xi'an, China

[2]Key Laboratory of MEMS/NEMS Systems of Shaanxi Province, 710072 Xi'an, China

[3]School of Mechanical Engineering, Northwestern Polytechnical University, 710072 Xi'an, China

[4]Department of Mathematical Sciences, Politecnico di Torino, 10129 Torino, Italy

[5]School of Aeronautics, Northwestern Polytechnical University, 710072 Xi'an, China

Corresponding author: Yang He, heyang@nwpu.edu.cn, Weizheng Yuan, yuanwz@nwpu.edu.cn

(Received xx; revised xx; accepted xx)

Flow around a submerged cylinder near a free surface reveals that adjusting the Froude number and gap ratio influences the underwater jet pattern, vortex shedding frequency, and free-surface deformation. The jet typically separates near the wave trough, leading to localized vorticity concentration and breaking waves that dissipate wake energy. In Antarctic waters, Type B killer whales employ a linear formation to generate a deep and smooth depression wave, breaking sea ice and washing seals from ice floes. Noting that killer whales raise their heads and swing their tails downward when approaching ice, we posit that this pitched posture enhances the tail-induced depression wave. This study investigates the wave-generating hydrodynamics using a towing tank and Particle Image Velocimetry. A scaled model with an elliptical body and rotatable wedge-shaped tail was tested under Froude similarity. Experiments covered towing speeds of 0.3 to 0.7 $\mathrm{m\,s^{-1}}$, combining different body pitch angles (10°/0°/−10°) and tail angles (30°/0°/−30°), at chord-based Reynolds numbers from 17 030 to 40 506. Four wake regimes are identified: small-scale vortex impingement induced by capillary waves; extensive wave breaking due to flow separation at the trough; smooth depression wave caused by downward advection of wake vortices and jet attachment; and large-scale vortex impingement generated by wake vortex perturbations. Results indicate that the posture with an upward-pitched body and downward-swept tail produced the most pronounced depression wave at 0.7 $\mathrm{m\,s^{-1}}$. The jet attached successively to the curved dorsal surface and the wave trough via the Coandă effect, suppressing flow separation and wave breaking at the trough. The strong jet maintained a low-potential-energy state in the trough. The depression wave caused large ice floes to flip and fracture through cantilever bending, while smaller ice floes were overwashed. The present findings—using a jet to reattach to a deformed free surface for wake optimization—suggest a novel flow-control strategy for objects near the free surface.

1. Introduction

The killer whale (*Orcinus orca*), the largest species in the family Delphinidae, can reach a body length of 6 to 9 m (Bester *et al.* 2017). Its natural distribution spans a wide range from the Arctic to the Antarctic waters(Blanc & Martínez-Rincón 2023). Orcas exhibit complex group behaviors and possess remarkable environmental adaptability (Baird & Dill 1996; Jefferson *et al.* 1991; Reisinger *et al.* 2015). As apex predators in the ocean, they occupy a unique ecological niche (Pitman *et al.* 2001; Blanc & Martínez-Rincón 2023; Pancaldi *et al.* 2024; Orellana-Vásquez *et al.* 2025). In Antarctic regions, Type B orcas primarily prey on seals, with local populations displaying striking social behaviors (Guinet *et al.* 2007; Reisinger *et al.* 2015). They hunt cooperatively, employing strategies such as wave-washing waves by rapid swimming to dislodge seals from ice floes (Smith *et al.* 1981; Visser *et al.* 2008). The Weddell seal (*Leptonychotes weddellii*) and crabeater seal (*Lobodon carcinophagus*) are primary prey of the Type B orcas (You *et al.* 2019). These seals predominantly inhabit flat, low-density first-year ice floes in the circumpolar Antarctic region, which are more accessible due to their regular shape and ease of climbing (Pitman & Durban 2012; Bester *et al.* 2017). They rely on these ice floes for breeding, rearing pups, and evading orca predation (Ackley *et al.* 2003). The predator-prey dynamics between orcas and seals largely revolve around sea ice interactions. Their highly intelligent behaviors may provide insights for human applications.

Early observations by Smith *et al.* (1981) documented orcas hunting a solitary crabeater seal. After assessing the hunting environment, a pod of seven orcas generated a powerful wave through coordinated swimming, tilting the ice floe at a steep angle and dislodging the seal into the water, where it drowned. This study qualitatively described the dynamic interplay between ice floes, waves, and orca behaviors. Visser *et al.* (2008) recorded six hunting events, detailing how orcas employed wave-washing to destabilize seals and fracture ice surfaces. However, these studies lacked deeper physical insights into wave generation mechanisms. Pitman & Durban (2012) provided a detailed account of wave-washing behavior. Prior to wave generation, subtle convex waves formed near the orcas' heads, while deeper concave waves emerged near their tails. The tight pod formation of orcas exerts notable effects on the free surface via synchronized locomotion and caudal fin-induced water displacement, suggesting the potential existence of underlying vital physical mechanisms. You *et al.* (2019) employed computational fluid dynamics (CFD) and recirculating flume tank experiments to investigate the wavelength and wave height generated by an elliptical cross-section model of a false orca under varying swimming speeds and depths. Their findings indicated that effective hunting waves are produced at speeds $\geqslant$ 3 m s^{-1} and depths of 0.4 to 1.1 m. However, their model oversimplified the dynamics by neglecting the influence of swimming attitude and the coupled effects of generated waves on ice floes (Fish 1998; Boutin *et al.* 2018).

Our observations of orca predation originate from some documentary films or open resources, e.g., *Frozen Planet* (Episode 1, BBC) and *Our Oceans* (Episode 5, Netflix). The documentaries use the terms 'crack' (26:20, *Frozen Planet*) and 'dismantle' (44:00, *Our Oceans*) to describe wave-induced damage to ice floes. Orcas employ fluid-structure interaction to first fracture the ice before encircling their prey. We observed that groups of orcas swim rapidly toward ice floes, generating a depression wave within seconds on otherwise calm water, right behind the pod. The wave height increases with swimming distance while maintaining a width slightly greater than the pod's formation. Based on our observations, orcas appear to deliberately raise their heads during hunting. While the full purpose of this behavior remains unclear, such as for improved visibility or breathing,

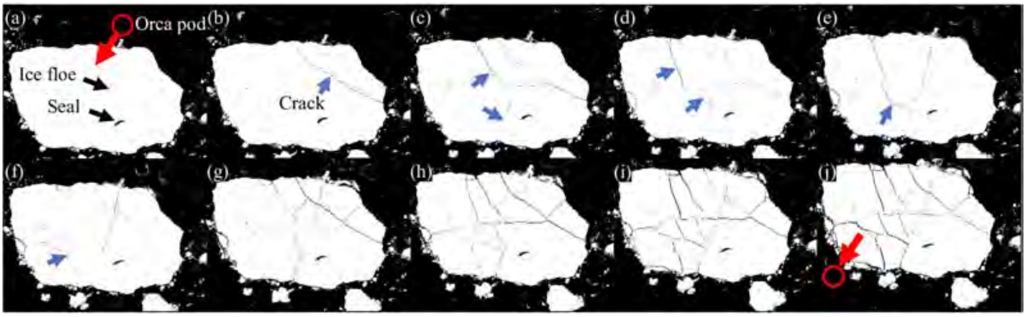

Figure 1. The time-sequenced panels illustrate crack propagation during the ice-breaking process, with an interval of approximately one second between adjacent frames. Red arrows indicate the pod's swimming direction, and red circles mark the orcas' positions. The blue arrows indicate newly formed cracks. Images were extracted from *Our Oceans* (Episode 5, 43:33 to 43:40), a documentary produced by Netflix.

we posited that this posture, combined with rhythmic downward tail slaps, may enhance wave-generation efficiency.

The wave propagation speed matches the orcas' swimming velocity. When the wave reaches the ice floe, the initial depression causes the leading edge to tilt toward the wave's center. For a larger ice floe, while the trailing edge remains horizontal, the leading edge experiences gravitational loading that induces bending stresses. Fracture occurs when these stresses exceed the ice's flexural strength. As the wave propagates, the depression continues to act on subsequent sections of the ice floe, producing radial cracks aligned with the wave's direction of travel. Figure 1 presents binarized snapshots showing four orcas fracturing a large ice floe. The primary cracks exhibit a radial pattern relative to the pod's approach direction, as shown in figure 1(j). Squire *et al.* (1995) described parallel fractures along ice shelf edges caused by incident ocean waves, which subsequently break into angular ice floes—a process sharing similarities with orca-induced fracturing, though the pod's narrower wave width likely explains the observed radial cracking. Smaller ice floes resist fracture due to strong inter-crystalline bonding (Mellor 1986) but experience pronounced tilting. The subsequent wave crest then impacts the inclined surface, generating sufficient kinetic energy to wash seals into the water. Currently, critical gaps remain in understanding how orcas generate hunting waves and how these waves mechanically interact with ice floes. The development of flow structures beneath ice floes and their fluid-structure interactions may be more complex than currently understood, warranting further quantitative investigation.

Based on the degree of freezing, sea ice can be classified into landfast ice, pack ice, marginal ice zone, pancake ice, nilas, and frazil ice (Squire 2020). The complex relationship between crystallization temperatures of different salts poses challenges in characterizing the mechanical properties of sea ice (Timco & Weeks 2010). During seawater freezing, the incompatibility between ice crystal lattice points and seawater ions results in stratified internal structures and varying microstructures within ice floes (Petrich & Eicken 2017). Under gravitational influence, the intermediate layer of columnar ice formed by the crystallization of free water at low temperatures dominates ice floes, exhibiting characteristic hexagonal patterns in horizontal cross-sections (Petrich & Eicken 2009). This intermediate layer profoundly influences the mechanical properties of ice floes. Although environmental factors (e.g., temperature affecting brine volume and pore geometry) and the ice's formation history may alter the material properties of natural sea ice, making comprehensive quantification of internal physical parameters difficult (Petrich & Eicken 2017), the intermediate layer still demonstrates significant directional

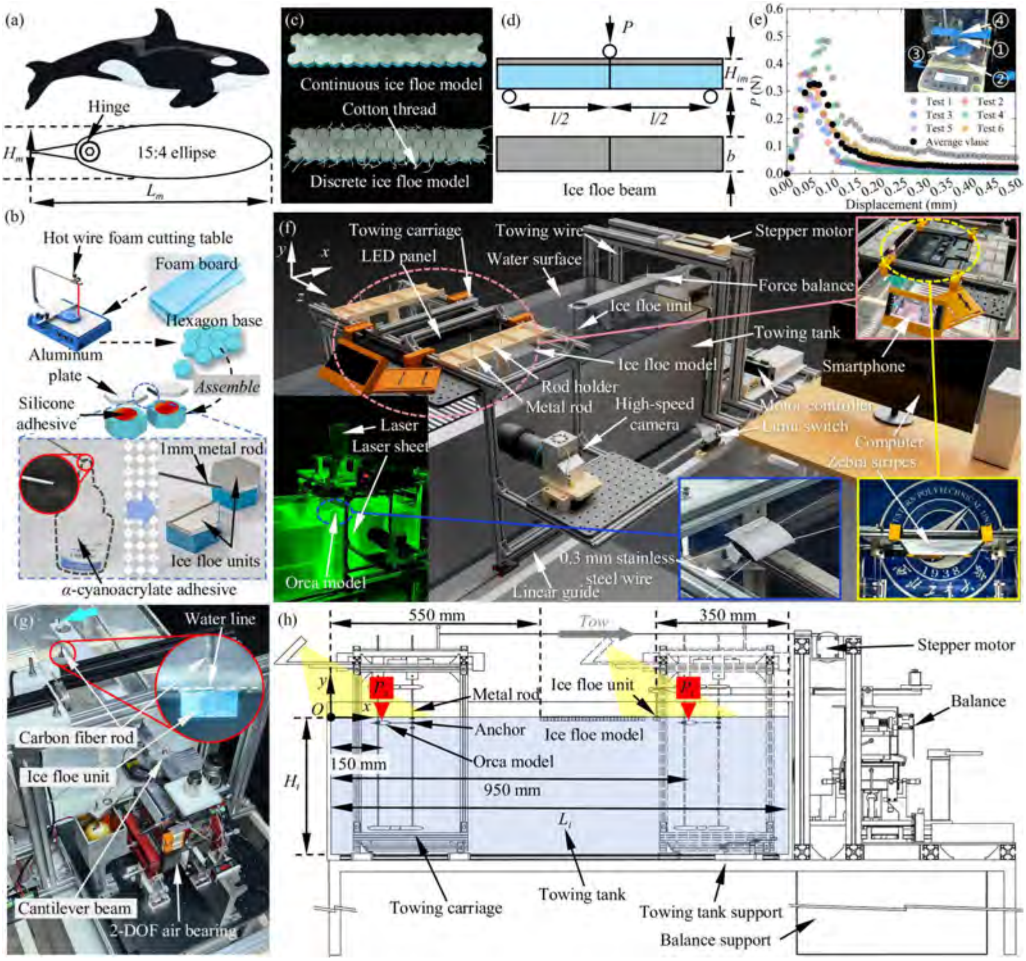

Figure 2. (a) Comparison between real orca morphology and simplified orca model. (b) Fabrication of ice floe unit. (c) The continuous and the discrete ice floe model. (d) Schematic diagram of the three-point bending test for ice floe beams. (d) Three-Point Bending Test. (e) The load-deformation relationship of the ice floe beam, displaying results from six independent measurements and their average values, also illustrating the measuring tools in the diagram: (1) fabricated ice floe beam, (2) precision balance, (3) base with 4.0 mm-diameter support rollers, and (4) force probe equipped with a ball-tip micrometer thimble (0.01 mm feed precision). (f) Experimental towing tank and related arrangements. (g) The three-dimensional micro-force measurement balance. (h) The side view of the towing tank clearly illustrates the installation relationships of the measurement devices and multiple critical dimensions. The edge of the upstream water surface in the towing tank is regarded as the geometric origin for describing key locations in the side view.

dependence, with elastic characteristics showing anisotropy (Petrich & Eicken 2009). For instance, tensile strength parallel to the growth direction of columnar ice can be three times greater than in the perpendicular direction (Timco & Weeks 2010), while deformation perpendicular to crystal columns is markedly greater than parallel deformation (Wang 1981). Compared to multi-year ice, first-year ice exhibits pronounced anisotropy (Timco & Weeks 2010). Ocean waves can induce bending in ice layers, forming ice-coupled waves or flexural-gravity waves (FGWs) that lead to ice fracture (Zemlyak *et al.* 2019; Squire 2020). In open water, FGWs may play a critical role in ice breaking.

When the load reaches a specific velocity, the frequency of flexural waves in the ice matches that of surface gravity waves, resulting in coupled FGWs capable of breaking ice (Kheisin 1967). Compared to studies on ice-breaking under impact or moving surface loads, research on FGWs generation by submerged moving objects remains limited (Pogorelova *et al.* 2018). Early experimental validation was provided by Kozin & Onishchuk (1994), demonstrating that submarine-induced FGWs could fracture ice. Pogorelova & Kozin (2011) conducted experiments measuring ice deflection under submarine models at varying submerged depths, water depths, and speeds, finding that reduced water depth increased FGW amplitude. Kozin & Zemlyak (2012) experimentally showed higher wave resistance beneath ice compared to free surfaces. Zemlyak *et al.* (2013) investigated submarine geometry effects, revealing that larger cross-sections improved ice-breaking efficiency. Zemlyak *et al.* (2018) studied length-to-diameter ratios and depth effects, concluding that ratio changes didn't reduce critical velocity (peak fracture occurred at critical speed), though increased ratios decreased wave curvature. Pogorelova *et al.* (2018) combined experiments and theory to examine water depth's influence on wave amplitude, demonstrating shallower depths lowered characteristic velocity while increasing wave height at low speeds. Zemlyak *et al.* (2022) analyzed surface displacement induced by near-surface/ice-proximity submerged bodies, quantifying ice layer effects on motion parameters. Pogorelova *et al.* (2019) modeled snow-covered ice using viscous oil layers atop elastic plates, showing that viscous damping significantly suppressed FGWs and reduced ice-breaking. Most recently, Zemlyak *et al.* (2023) experimentally and theoretically studied shallow submerged body forces and ice-breaking capacity in finite-depth water. A broader methodological context is provided by Squire (2011), who cataloged modeling approaches for elastic plate responses under complex ice parameters. Ni *et al.* (2024*a*) reviewed theoretical/numerical studies on submerged moving object ice-breaking. Such research typically simplifies either the object (ice as elastic plates, bodies as source-sink systems) or flow conditions (inviscid potential flow) to enable analysis convergence ((Bukatov & Zharkov 1995; Kozin & Pogorelova 2008; Das & Mandal 2010; Lu & Dai 2008; Pogorelova & Kozin 2010; Pogorelova 2011; Sturova 2012, 2013; Pogorelova & Kozin 2014; Li *et al.* 2017; Ni *et al.* 2020, 2024*b*; Xiong *et al.* 2025). Current numerical studies predominantly suffer from oversimplified wave-ice interactions, attempting to model attenuation and diffusion effects within linear wave theory while entirely neglecting nonlinear vortex structures.

Unlike conventional ice-breaking methods, orca pods form a distinctively wide disturbance array, generating relatively independent waves that constitute a previously unrecognized ice-breaking mechanism different from wind, waves, or collisions (Montiel & Squire 2017). The waves produced by orcas exhibit significantly higher wave-height-to-wavelength ratios compared to those generated by atmospheric, oceanic, or submarine forces. Seal-inhabited ice floes typically feature characteristic dimensions much smaller than the wavelengths excited by either ocean waves or elongated submarine models. Consequently, their elastic responses may differ substantially from those of infinite/semi-infinite ice sheets, with flexural wave effects potentially less pronounced. Inspired by natural hunting strategies, the orca's behavior can be categorized into three phases: 1. Reconnaissance: steady subsurface swimming for environmental assessment. 2. Fragmentation: high-energy swimming to fracture large floes into smaller pieces. 3. Prey dislodgement: targeted wave generation to wash seals off fragmented ice. Crucially, swimming posture may determine ice-breaking efficiency. In this study, we experimentally investigated the mechanism of wake depression waves generated by an orca model under different postures, and reproduced and validated the ice-breaking strategies of orcas using artificially fabricated floating ice models. The paper is structured as follows. Section 2 comprehensively introduces the

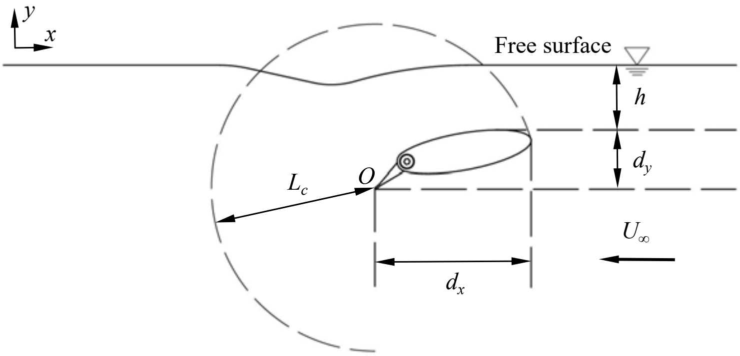

Figure 3. Overview of experimental arrangement and definition of flow and geometrical parameters.

experimental setup and measurement tools. Section 3 details the findings, explaining the wake regimes observed over the entire tested velocity range; in particular, Sections 3.1 and 3.2 focus on the classification of wake regimes and the characteristics of the time-averaged flow field, instantaneous flow field, time-averaged vorticity, swirling strength vector field, and velocity profiles at specified locations. Sections 3.3 and 3.4 describe the capsizing effects of depression waves on large and small ice floes, as well as the force conditions of ice floe units in complex environments. Finally, Section 4 summarizes the main findings and implications of this study.

2. Experimental set-up

2.1. *Orca model*

According to the study of Kozin & Onishchuk (1994), the length of orca L_o scales linearly with the model length L_m:

$$L_o/L_m = \lambda_l. \tag{2.1}$$

The wavelength and amplitude of the waves also follow this scaling relationship:

$$\lambda_o/\lambda_m = A_o/A_m = \lambda_l, \tag{2.2}$$

where λ_o and λ_m represent the wavelengths of waves generated by real and model orcas, respectively, while A_o and A_m denote the corresponding wave amplitudes. The orca model was designed based on a scaled-down simplification of the real orca, featuring an elliptical cross-section with a major-to-minor axis ratio of approximately 15:4. The tail was modeled as a rotatable thin triangular plate, with a 0.5 mm thick rectangular cross-section edge reinforcement at its tip for enhanced structural integrity. The tail-to-body length ratio was set at 1:5. The tail and body were connected via an articulated hinge positioned at the posterior of the elliptical section, where hinge tightness could be adjusted to modify the tail angle. The orca's tail fluke can achieve an oscillation amplitude of up to 60°. Accordingly, the hinge allows tail to be adjusted within a ±30° range, relative to the central plane of the body. Remaining flippers and dorsal fin were geometrically simplified (figure 2(a)).

	Prototype	Model
Length (m)	5.6	0.05
Velocity (m s^{-1})	$3.67 \sim 7.33$	$0.30 \sim 0.70$
Froude Number	$0.50 \sim 0.99$	$0.43 \sim 1.00$
Weber Number	$1.06 \times 10^6 \sim 4.25 \times 10^6$	$62 \sim 336$

Table 1. Comparison of physical parameters between the real orca and the model.

Since the orca swims near the water surface, both Froude number and Weber number were considered, calculated as:

$$\mathrm{Fr} = \frac{U_\infty}{\sqrt{gL}}, \tag{2.3}$$

$$\mathrm{We} = \frac{\rho U_\infty^2 L}{\sigma}, \tag{2.4}$$

where U_∞ represents the towing speed, and L denotes the characteristic length (taken as the total length of the research object). The gravitational acceleration g is 9.81 m s^{-2}, seawater density ρ is 1.03×10^3 kg m^{-3}, and surface tension coefficient σ is 0.073 N m^{-1}. The swimming speed range (3.67 m $s^{-1} < U_\infty <$ 7.33 m s^{-1}) and average length of the orcas (L_o = 5.6 m) were adopted from the study of You *et al.* (2019), who determined L_o based on the average length of predominant female orca and derived the speed range from video analysis (Visser *et al.* 2008).

Model dimensions and velocities were scaled using Froude number similarity (table 1). The orca model had a body length of 41.7 mm, tail length of 8.3 mm (total length L_m = 50.0 mm) and height H_m of 11.1 mm. The spanwise width (W_m = 55.5 mm, 5 times of model height) simulated the collective width of a 4 to 5 orca group. At flow speeds of 0.3 to 0.7 m s^{-1}, the Weber number ranged 62 to 336 $\gg 1$; thus, surface tension effects on wave generation were neglected (You *et al.* 2019).

The orca model was fabricated using 3D-printed black photopolymer resin. Longitudinal through-holes (0.5 mm diameter) were incorporated along the model's spanwise direction. A 0.3 mm stainless steel wire was threaded through these internal holes and secured to 3.0 mm metal anchor rods mounted near the towing tank sidewalls, which connected to the overhead towing carriage. During model installation, pliers were used to tension the steel wire, and after achieving sufficient tautness, the free end was secured with an aluminum wire sleeve clamp. The pre-tension force in the wire effectively minimized model vibration. The above arrangement eliminated flow field disturbances from support structures as much as possible. Body pitch angle was adjusted by varying the anchor points' relative heights on the rods, with positive angles defined by leading-edge upward tilt. Tail inclination (positive when uptilted) indicated the primary fluke orientation during water propulsion. Refer to table 2, multiple representative orca postures, from Cases 1 to 9, were systematically combined. Regardless of the installation configuration, the vertical distance h between the dorsal high point of the orca body and the water surface was maintained approximately $2H_{im}$ between the starting position (P_s) and the termination point (P_t). The ratio of h/d_y in table 2 is equally important, as it reflects the model's relative submergence depth. This relative position is annotated in figure 3. The orca model features a non-axisymmetric cross-section with significant differences in the x- and y-directions. Therefore, two orthogonal projection distances, d_x and d_y, are considered to define corresponding Froude numbers,

Case	Body angle (°)	Tail angle (°)	L_c (mm)	h/d_y	Re_c ($\times 10^4$)	Diagram
1	10	0	50.00	1.53	1.74 ~ 4.05	
2	10	30	49.05	1.53	1.70 ~ 3.97	
3	10	-30	49.05	1.13	1.70 ~ 3.97	
4	0	0	50.00	1.80	1.74 ~ 4.05	
5	0	30	49.05	1.67	1.70 ~ 3.97	
6	0	-30	49.05	1.60	1.70 ~ 3.97	
7	-10	0	50.00	1.53	1.74 ~ 4.05	
8	-10	30	49.05	0.88	1.70 ~ 3.97	
9	-10	-30	49.05	1.53	1.70 ~ 3.97	

Table 2. Statistics of orca model postures under varying body angles and tail angles.

Fr_x and Fr_y. The former one is expected to influence the coupling between the wake vortex structure and the free surface, while the latter primarily governs the free surface wave pattern deformation and is directly related to the volume of fluid displaced by the body and the pressure disturbances, which propagate as gravity waves on the free surface.

$$\mathrm{Re}_c = \frac{\rho U_\infty L_c}{\mu}. \tag{2.5}$$

Furthermore, the Reynolds number for the orca model in flow also needs to be considered. As given in equation 2.5 and using the chord length L_c as the characteristic length, the Reynolds number was calculated. In the equation, the dynamic viscosity μ is 8.9×10^{-4} Pa s, and L_c is defined as the distance between the endpoints of the tail and the head, as illustrated in figure 3. Both L_c and Re_c are listed in table 2. The values confirm that the model's motion occurs within a turbulent wake flow regime. The instantaneous streamwise (x-axis), normal (y-axis), and spanwise (z-axis) velocity components at any point in the flow field are denoted as u, v, and w, respectively. These are composed of the superposition of the local mean velocities $\bar{u}$, $\bar{v}$, $\bar{w}$, and their corresponding fluctuating components u', v' and, w'. The resultant velocity at a point in the flow field should be understood as the vector sum of its component velocities, i.e., $U = \sqrt{u^2 + v^2 + w^2}$. This study mainly analyzes the velocity field on the central plane of the model. Considering symmetry, the contribution of the spanwise velocity component on the centerplane of the model is neglected; therefore, the spanwise velocity component w is scarcely discussed in this paper. Further explicit reference to the meaning of symbols will be omitted in subsequent sections.

2.2. *Ice floe model*

Visser *et al.* (2008) reported ice-breaking widths of 4.5 to 18.0 m for orca groups, with maximum floe diameters reaching approximately 25 m and ice thickness ranging from below 0.5 m to over 1.5 m. Smith *et al.* (1981) observed floe diameters between 5 and 15 m. The dimensions and mechanical characteristics of model ice must still satisfy the scaling relationship. Based on actual proportions, 1/5 of the orca model length L_m was selected as the model ice thickness $H_{im} \approx 10$ mm. The corresponding natural ice thickness can be estimated by the following equation:

$$H_{in} = H_{im}\lambda_l^{4/3}\left([\sigma_u]_n / [\sigma_u]_m\right)^{-1/3}, \tag{2.6}$$

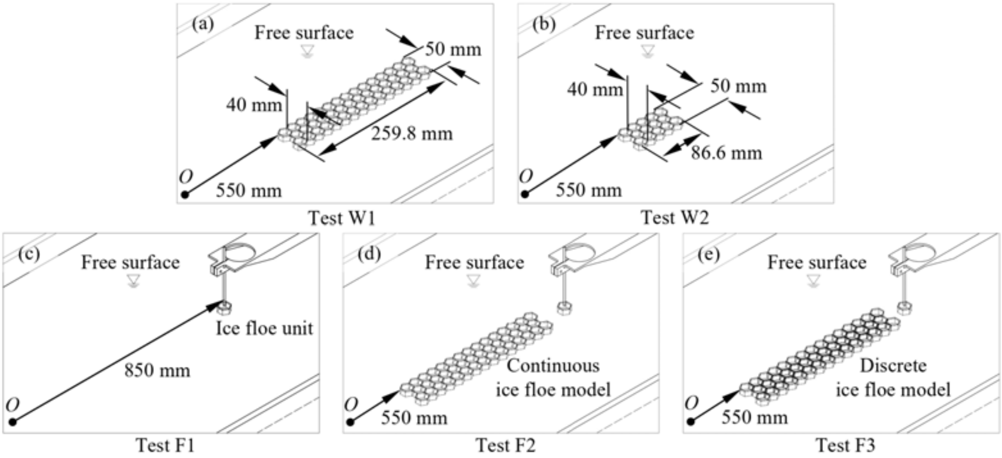

Figure 4. (a) and (b) illustrate the parameter configurations for experiments on wave-induced overturning of large and small continuous ice floe models. (c), (d) and (e) present the parameter configurations for experiments measuring the three-dimensional micro-force response of an ice floe unit under wave action. In (c), only the force on the isolated ice floe unit is measured. In (d) and (e), continuous and discrete ice floe models are placed upstream of the target unit. In all experiments, the ice floe unit, ice floe models, and orca model must be aligned on the same central plane. During preparation, the water surface must remain calm, and the positions of the ice floes must be carefully adjusted.

where H_{in} and H_{im} represent the thicknesses of natural ice and model ice, and $[\sigma_u]_n$ and $[\sigma_u]_m$ denote the flexural strengths of natural ice and model ice, respectively. Using the upper limit of sea ice flexural strength reported by Timco & O.'Brien (1994) as the reference value ($[\sigma_u]_n \approx 1.50$ MPa), the flexural strength of the model ice was designed as $[\sigma_u]_m \approx 9.53$ kPa to simulate natural ice thickness $H_{in} \approx 1/5L_o$.

As shown in figure 2(b), the ice floe substrate was fabricated using polystyrene foam boards cut into 10 mm regular hexagonal units (density of 0.42 g cm^{-3}) to simulate columnar ice cross-sections. Waterproof silicone adhesive was applied to bond hexagonal aluminum plates (density of 2.80 g cm^{-3}) of identical dimensions atop the foam units. When the aluminum plate thickness was $1/5H_{im}$ and the foam thickness $4/5H_{im}$, the model ice density reached 0.90 g cm^{-3}, which approximating real ice conditions (Dumont *et al.* 2011), with approximately $1/10$ of its height exposed above water (Squire 2011). The large continuous ice floe model was assembled from small hexagonal ice units bonded with α-cyanoacrylate adhesive. The adhesive was applied to the side surface of the aluminum plate using 1 mm diameter metal rod, with transfer conditions deemed satisfied when the adhesive sufficiently wetted the rod's end surface. The adhesive-coated surfaces were then brought into contact with the aluminum plate sides of adjacent ice units and rapidly clamped for curing. As shown in figure 2(c), the large continuous ice floe model consisted of 44 units arranged in three columns: the first and third columns each consisted of 15 units, while the middle column contained 14 units. We also fabricated a discrete model, where individual ice units maintained gaps of approximately 1 mm and were interconnected with cotton threads. This discrete configuration was designed to simulate small ice floe groups consisting of fragmented but closely spaced floating ice pieces. It should be noted that the slender layout ignores the three-dimensional effects to some extent, focusing on the effect of the trailing waves generated by the orca model near its central plane on the floe.

Figure 2(d) illustrates that the equivalent flexural strength between bonded units was estimated via three-point bending tests (Timco & O.'Brien 1994), with loading applied parallel to adhesive seams at a constant rate. The flexural strength is expressed as:

$$\sigma_f = \frac{3Pl}{2bH_{im}^2}, \tag{2.7}$$

where P is the applied load, $l = 40$ mm denotes the support span of the ice floe model beam, and $b = H_{im} = 10$ mm represents the width and height of the hexagonal ice model, respectively. As shown in figure 2(e), six independent measurements of the flexural strength of the ice floe beam were conducted. The mean results demonstrated that the beam exhibited linear deformation under loading until fracture occurred at displacements exceeding 0.06 mm, with a maximum recorded load of approximately 0.33 N. While initial deformation stages exhibited excellent reproducibility, displacement-dependent divergence emerged, likely due to variations in α-cyanoacrylate wetting and curing. The derived flexural strength at peak load was $\sigma_f \approx 19.80$ kPa $> [\sigma_u]_m$. Notably, flexural strength parameters display inherent variability influenced by hydrographic conditions, brine volume, ice temperature, and loading rate (Han *et al.* 2016). Elevated temperature or brine content reduces strength, with young ice exhibiting higher strength than aged ice (Fransson 2002). Reported sea ice flexural strengths range 0.1 to 1.5 MPa (Timco & O.'Brien 1994). The artificial ice floe models in this study may simulate thicker ice than intended (i.e., ice floe with s thickness of 1.27 m), though all values remain within physically plausible ranges.

In all experiments presented in this study, the leading edge of the ice floe model was positioned 550 mm downstream in the towing tank. Figure 4(a) and (b) illustrate the experimental setups for investigating wave-induced tilting effects on large continuous ice floes (arranged in a 15×14×15 array) and small continuous ice floes (arranged in a 5×4×5 array). High-speed cameras were employed to capture snapshots of the ice floe overturning process. Figure 4(c) depicts the force measurement setup for waves acting on an isolated ice floe unit (positioned 850 mm downstream in the towing tank). In configurations (d) and (e), modifications were made by placing continuous and discrete large ice floes upstream of the target unit to evaluate the dissipation effect of large intact ice floes or dense and discrete ice arrays on subsequent wave forces. A custom-designed force balance was used for force measurements. Further details regarding the high-speed camera and the force balance are provided in subsequent sections.

2.3. *Towing tank and flow field visualization system*

The experiments were conducted in W. Zhou's wind tunnel laboratory at the School of Mechanical Engineering, Northwestern Polytechnical University. As illustrated in figure 2(f), all towing experiments were conducted in a custom-built transparent acrylic water tank with internal dimensions of $L_t = 24.0L_m$ (length), $W_t = 9.1W_m$ (width), and $H_t = 32.4H_m$ (water depth). Under these parameters, sidewall effects on wave generation were negligible, and deep-water conditions were satisfied. The laboratory is equipped with an air conditioning system to maintain a constant temperature of 25 ± 1°C. Given the significant difference in viscosity between air and water at room temperature, the influence of air on the water flow is neglected to approximate the conditions of a free surface. Two 1200-mm-long linear metal rails were installed along the tank sides. A towing carriage, constructed from 2020 aluminum profiles with redundant structural reinforcement, was mounted on the rail sliders. The carriage featured dual rod holders, each securing two 3-mm-diameter, 550-mm-long stainless steel rods positioned approximately 30 mm from the sidewalls, perpendicular to the water surface. The carriage was towed via 1-mm steel cables driven by a stepper motor at the tank end. Towing speed was calibrated using high-speed imagery and scale markers. Calibrated anchor points on the rods enabled model pitch adjustment. An LED panel (modified to display 10 mm black/white zebra stripes) was mounted atop the carriage. A smartphone (Huawei P60 Art), fixed via a customized holder (orange one in the upper-right subplot), recorded reflected patterns at 4K/60 fps to quantify free-surface deformation and corresponding wake scars and striations(3840×2160 pixels). The smartphone position was adjusted to maximize pattern coverage. A high-speed camera (Cyclone-2-2000 M, Optronics; lens: AF-S Nikkor 24-120 mm f/4 ED VR, Nikon) was mounted laterally on a platform to capture horizontal free-surface snapshots (1920×1080 pixels) at the model centerplane and the total field of view is approximately 220 mm×70 mm ($x \times y$). The camera sampling rate is set to 250 Hz. For particle image velocimetry (PIV), the LED panel was replaced with a 7.5 W maximum power continuous laser (532 nm, 5W-EC31811, Changchun New Industries Optoelectronics Tech. Co., Ltd.) generating a 0.5-mm-thick light sheet (30° divergence angle) aligned with the orca model's centerplane (see bottom-left subplot of figure 2(f)). A black velvet cloth was attached to the outer surface of the acrylic water tank wall opposite the high-speed camera to improve image quality and reduce unwanted laser reflections. Due to the mechanical structure of the support frame, the laser sheet was incident on the water surface from the top. The refraction from the deformed free surface introduced minor perturbations to the instantaneous velocity field at the wake interface, where vortex structures frequently impinged. However, the averaged results demonstrated a convergent trend, but it is still recommended that future studies employ a bottom-incident laser sheet. The rod holder of the towing carriage caused minor obstruction in the PIV sampling area, potentially introducing errors in cross-correlation calculations near the obscured edges. Nevertheless, these regions were readily identifiable and did not affect the conclusions of this study. The water was seeded with 50 μm polyamide resin particles (PSP; refractive index: 1.56; density: 1.03 g cm^{-3}), and the camera was repositioned horizontally relative to the model, with the sampling rate set to 2000 Hz. PIV data were processed using the PIVLab software package (version 3.06). A final interrogation window of 8×8 pixels with 50% overlap was used to satisfy the Nyquist criterion. Instantaneous and ensemble averaging of the flow velocity vectors was performed using a cross-correlation algorithm. The time-averaged quantities were obtained from 500 frames of the instantaneous velocity field. All imaging stations were positioned within the fully developed flow region, approximately 700 mm downstream of the towing tank. A three-dimensional micro-force balance was positioned externally downstream of the towing tank. To isolate the measurement system from vibrations induced by towing dynamics, the force balance was mounted on an independent vibration-damping support. The balance's sensing probe was fitted with an ice floe unit through a carbon fiber rod, positioned 850 mm downstream of the towing tank edge. The limit switch installed beside the rail ensured consistent travel (between $P_s = 150$ mm and $P_t = 950$ mm from the upstream edge), with the orca model having fully cleared the ice structures before motor deceleration was triggered. Additional tank details are provided in figure 2(h).

2.4. *Decoupling-free balance for three-dimensional micro-force measurement*

As shown in figure 2(g), a custom-designed decoupling-free three-dimensional micro-force balance was used to measure the micro-mechanical responses of an isolated ice floe unit under wave action. The ice floe unit was fixed to the end of a 3-mm-diameter carbon fiber rod, which was clamped to the front end of the balance's measuring probe (configured as a cantilever-beam lever). When hydrodynamic forces act on the ice floe unit, the force signals are transmitted through the cantilever beam to the balance for measurement.

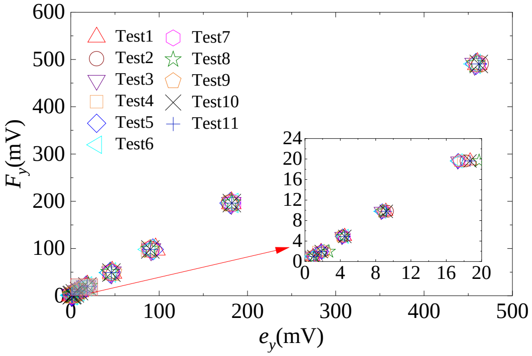

Figure 5. Calibration results along y axis. F_y denotes the reference force applied along the y-axis, generated by Class F1 standard weights, while e_y represents the voltage transducer output reading.

The balance operates on an air-floating principle, with its core component being an independently designed two-degree-of-freedom (2-DOF) air-bearing platform. The mechanical structure was inspired by the one-dimensional air bearing proposed by Zhou *et al.* (2025). When high-pressure gas is supplied, the air bearing achieves gas lubrication, reducing the frictional resistance of moving parts to negligible levels. The 2-DOF air bearing provides pre-decoupled force measurement in the horizontal x- and z-axes. The forces are calculated by measuring the micro displacements of the air-bearing slider in orthogonal directions within the horizontal plane, combined with the stiffness coefficients of elastic elements. The y-axis force is measured using a stress-strain sensor, with the lever structure enhancing force measurement resolution. The moving components of the balance are free from interference by external cables or mechanical structures, enabling pure three-dimensional micro-force measurements. The stiffness coefficients of the balance in the x- and z-axes are 23.451 N m^{-1} and 25.458 N m^{-1}, respectively. Given the use of an infrared laser sensor with 0.5 µm resolution to measure micro-displacements, the force resolutions in these directions are approximately 1.17×10^{-5} N and 1.27×10^{-5} N, with measurement ranges of ±0.31 N and ±0.19 N, respectively. The combined uncertainties in each direction arise from the laser sensor and elastic elements, resulting in relatively expanded uncertainties of 0.68% and 0.33% for the x- and z-axes, respectively.

For the y-axis, the cantilever beam was modified with an extended length, and the position of the stress-strain sensor was altered, necessitating recalibration. Nine different Class F1 standard weights were sequentially and steadily placed at the probe's end, with the central axis of the weights aligned with the centerline of the carbon fiber rod mounting hole (indicated by a thick cyan arrow in figure 2(g)). The raw calibration data are presented in figure 5, and the results of 11 independent calibration tests are summarized in table 3. The stiffness coefficient was determined as the mean slope of the 11 calibration lines:

$$\bar{k}_y = \frac{\sum_i^n k_{yi}}{n}, n = 11, \tag{2.8}$$

thus, $\bar{k}_y = 1.0671$ N V^{-1}, with a resolution of approximately 1.07×10^{-4} N and a measurement range of ±0.6 N. The uncertainty of each independent calibration can be expressed by the residual standard deviation r_y:

$$u\left(k_y\right) = \frac{r_y}{\sqrt{\sum_{i=1}^n \left(e_{yi} - \bar{e}_y\right)^2}}, n = 9, \tag{2.9}$$

n	k_y (N V^{-1})	R^2	r_y (N)	$u\left(k_y\right)$ (N V^{-1})
1	1.0671	0.9999	1.8172	0.0043
2	1.0607	0.9999	1.9873	0.0046
3	1.0726	1.0000	0.5836	0.0014
4	1.0669	0.9999	1.6900	0.0040
5	1.0696	0.9999	1.2716	0.0030
6	1.0709	1.0000	1.0620	0.0025
7	1.0650	1.0000	0.7054	0.0017
8	1.0716	1.0000	1.0939	0.0026
9	1.0693	0.9999	1.5679	0.0037
10	1.0630	1.0000	1.1858	0.0028
11	1.0659	0.9999	1.3569	0.0032

Table 3. The results of the fitted stiffness coefficient k_y, goodness-of-fit R^2, residual standard deviation r_y, and uncertainty $u\left(k_y\right)$.

where r_y can be calculated as follows:

$$r_y = \sqrt{\frac{\sum_{i=1}^{n}\left(\left(F_y\right)_i - \left(F_y\right)_{0i}\right)^2}{n-2}}, n = 9. \tag{2.10}$$

In equations 2.9 and 2.10, n represents the number of different standard weights applied during an independent calibration, e_{yi} denotes the voltage reading difference before and after applying the i-th weight force $\left(F_y\right)_i$, $\bar{e}_y$ is the mean value of e_{yi}, and $\left(F_y\right)_{0i}$ represents the calculated value corresponding to e_{yi} on the fitted line. The uncertainty of $\bar{k}_y$ is expressed as:

$$u\left(\bar{k}_y\right) = \sqrt{\frac{\sum_{i=1}^{n} u\left(k_y\right)_i^2}{n\left(n-1\right)}}, n = 11, \tag{2.11}$$

here, n represents the number of independent calibrations, and the relative uncertainty of $\bar{k}_y$ can be expressed as:

$$u_r\left(\bar{k}_y\right) = \frac{u\left(\bar{k}_y\right)}{\bar{k}_y}. \tag{2.12}$$

The calculated uncertainty of $\bar{k}_y$ is approximately 0.001 N V^{-1}, corresponding to a relative uncertainty of 0.1%. The balance operates at a sampling rate of 10 Hz, with triaxial force signals transmitted to a microprocessor via LoRa wireless protocol before being collectively relayed to a computer. Testing confirmed that the system's clock drift remains below 10 ms over 20-minute operation periods. The influence of sampling circuitry on measurement results was negligible. For additional technical details regarding the balance, refer to the work by Zhou *et al.* (2026).

3. Results

3.1. *Free-surface depression wave*

Figure 6 presents the wave patterns on the central plane of the model for Cases 1 to 9 under towing speeds of 0.3 to 0.7 m s^{-1}. The contour points were obtained from the

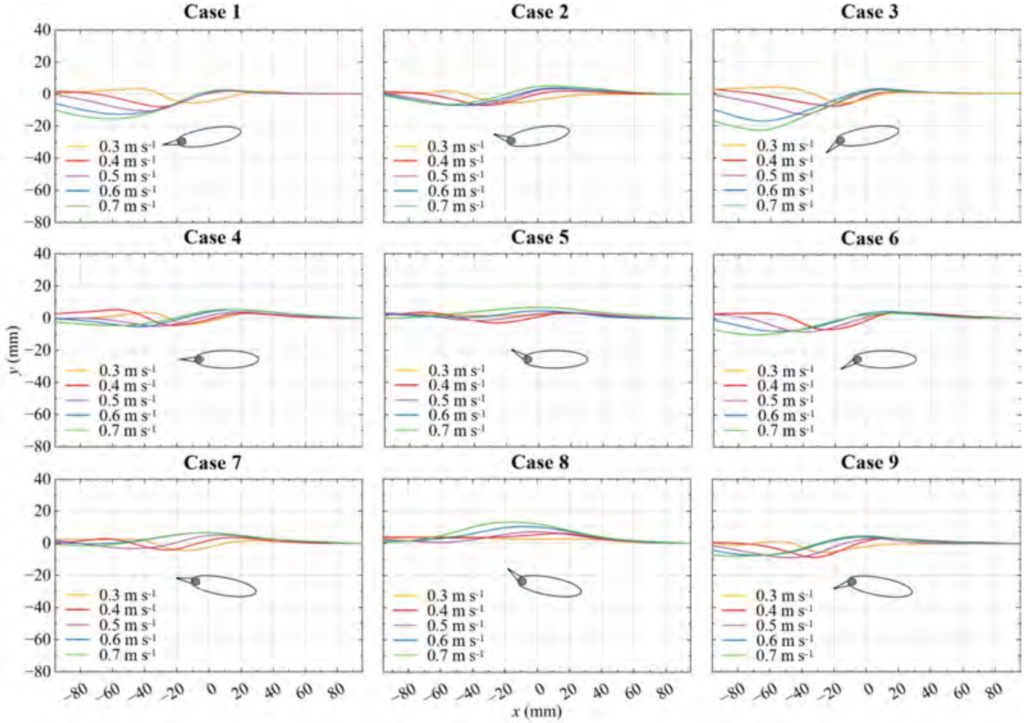

Figure 6. The free surface deformations under different cases and towing speeds are investigated. The background grid is solely used for evaluating surface deformation and is not associated with a specific reference position.

averaged statistical results of multiple stacked image frames. Spline curves defined by control vertices were used to connect the contour points, which were then transferred to a grid plot. This process temporarily neglected small-scale fluctuations of the liquid surface, thereby illustrating the macroscopic deformation of the free surface. Distinct differences in wave patterns are observed among the cases, with both the body and tail parts of the orca model influencing wave development.

Cases 1 to 3 all produced readily identifiable free-surface depression waves. The depression wave in this article specifically refers to the first trough appearing behind the model. The depression wave in Case 3 was the most pronounced, reaching a depth of 22.8 mm at 0.7 m s^{-1}, followed by Case 1, which generated a depression wave of 15.9 mm at the same speed—the former being approximately 1.4 times deeper than the latter. The streamwise positions of the wave troughs (with the leading edge of the orca model's head as the origin) were 86.6 mm downstream for Case 3 and 81.3 mm downstream for Case 1. However, when the model's tail was uptilted (Case 2, 5, 8), the depression wave was significantly suppressed, affecting both the trough depth and its streamwise position. In Case 2, the maximum trough depth was only 7.2 mm, located at 74.1 mm downstream, under a towing speed of 0.7 m s^{-1}.

In Cases 4 to 6 and 7 to 9, downward flipping of the tail resulted in more pronounced tail depression waves. Conversely, uptilting the tail suppressed the depression wave. Inter-group comparisons indicate that the wave depth and streamwise position in these cases are all smaller than those in Cases 1 to 3. Additionally, localized elevations of the liquid surface above the undisturbed free surface were observed in Cases 5 and 8, to the extent

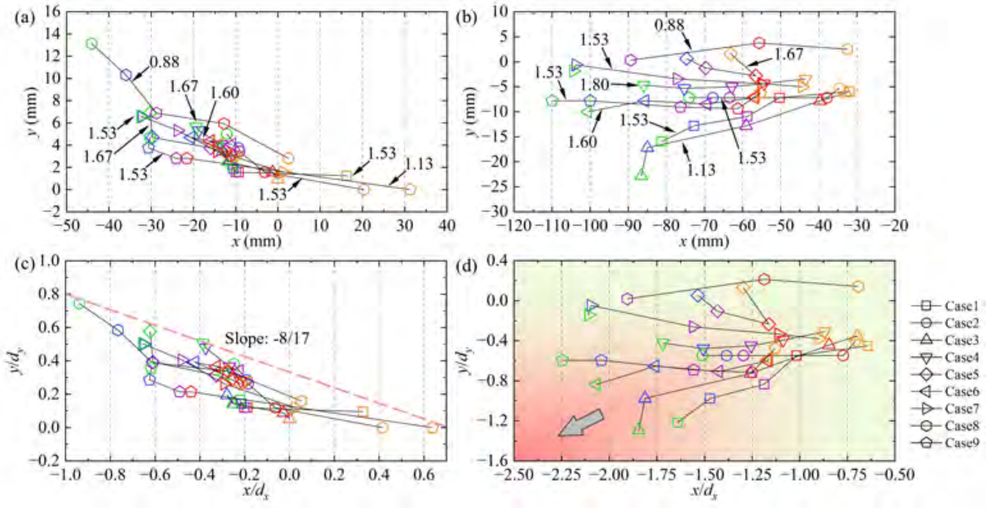

Figure 7. (a) and (b) show the positional data of the head wave crest and stern wave trough under different cases and towing speeds, respectively. (c) and (d) present the corresponding data normalized using d_y and d_x for the peak and trough points, respectively. '$-$' indicates being below the calm water surface or downstream of the leading-edge reference point of the model. The color of the symbols in the figure represents different towing speeds, consistent with figure 6.

that in Case 8, the depression wave even rose above the free surface. This is often attributed to a locally increased Froude number above the model, where exceeding a critical value can induce a hydraulic jump. This Froude number is determined by the local velocity U and local liquid height h_l, i.e., $\mathrm{Fr}_l = U/\sqrt{gh_l}$, which will be further explained later. More broadly, the depression wave depths in Cases 5, 7, and 8 were all relatively small, with troughs close to the free surface, and uptilted tails were a common feature among these three cases.

The bulge wave generated at the model's head also attracts attention, primarily influenced by the blockage effect at the model's frontal stagnation point. The height of the bulge wave is related to both h/d_y and the towing posture. Most bulge wave peaks are located 10 to 20 mm downstream of the model's leading edge. Case 8, with the smallest $h/d_y = 0.88$, produced the most prominent bulge wave, reaching a peak height of 13.1 mm at 0.7 m s^{-1}, situated 44.1 mm downstream of the head. In contrast, the wave heights in other cases were relatively moderate. Cases 1 and 3 exhibited the least sensitivity to bulge wave generation, with minimal variation in wave height with towing speed and limited streamwise displacement. As towing speed increased, the downstream shifting of the bulge wave slowed. An upward tilt of the head mitigated the blockage effect, thereby suppressing the growth of the bulge wave. Cases 5, 7, 8, and 9 showed relatively larger streamwise displacement ranges of the bulge wave. Among these, Case 5 featured an uptilted tail, while Cases 7 to 9 involved a downward pitching of the body. Their common feature is the deflection of the dorsal flow toward the water surface, which contrasts sharply with Cases 1 and 3. Figure 7(a) and (b) present the parameter distributions of the trough behind the model and the bulge wave peak, respectively, with the relative submergence depth annotated in (a) for reference.

Figures 7(c) and (d) present the normalized wave trough and peak positions in the normal direction and the streamwise position. In figure 7(c), the peak points exhibit a more uniform distribution pattern. All data points lie below a straight line with a slope of $-8/17$, showing a compact distribution. The slope reflects the trend of the peak position variation

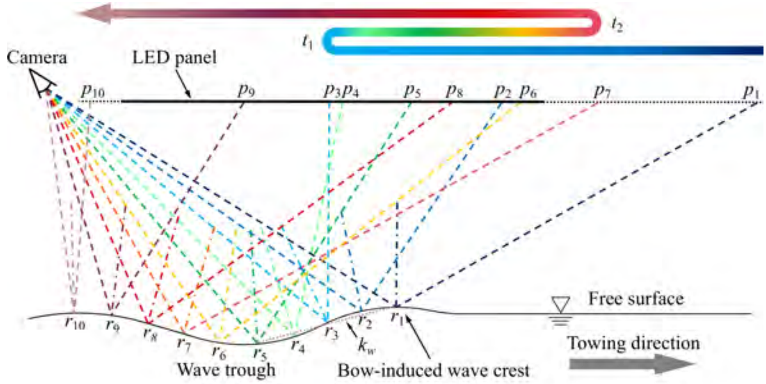

Figure 8. Optical path diagram of zebra stripes on the LED panel reflected by the wave surface. In this optical path diagram, the selected reflection points r_i $(i = 1 \sim 10)$ maintain similar spacing, while the positions of projection points p_i undergo nonlinear changes due to the curvature of the free surface. The colored arrow above reflects the movement trend of the projection points in the camera, and the camera's shooting vector reverses direction twice (marked as t_1 and t_2). The slope k_w of the line connecting the wave crests and wave troughs in the figure is used to evaluate the depression degree of the waves. The figure is not drawn to scale strictly.

with towing speed. The physical significance of this line lies in the constraint imposed by the orca's attitude on the bulge wave peak, indicating that a higher bulge wave peak cannot form further upstream. This relationship satisfies:

$$\frac{y}{d_y} < -\frac{8}{17}\frac{x}{d_x} + \frac{28}{85}. \tag{3.1}$$

Conversely, Cases 1, 3, and 9 lie at the lower-left outermost side of the line, indicating that these three cases exhibit stronger suppression of the bulge wave compared to most other conditions. Similarly, in figure 7(d), only the curves of Cases 1, 3, and 6 continue to show a proactive downward trend in the lower-left corner. As the towing speed increases, the stern depression wave further deepens. A common feature of these three cases is their downward-tail configuration.

Figures 9 to 11 provide further information on the free surface deformation through the zebra-stripe patterns. For an overview of the reflective pattern method used to measure free surface deformation, refer to the review by Gomit *et al.* (2022). In this study, the LED panel and smartphone lens were fixed relative to the towing carriage to capture the images of the surface deformation during the towing process. Before focusing on results, it is necessary to clarify the influence of wave peak and trough on the reflective stripes. Figure 8 illustrates a simplified two-dimensional relationship among the camera, LED panel, waves, and optical path. Although the elements are not drawn strictly to scale, the diagram is sufficient for explanatory purposes. Ten equally spaced reflection points r_i $(i = 1 \sim 10)$ were selected on the deformed surface. The reflected light paths from these points to the camera were constructed, and their intersections with the plane of the LED panel are denoted as corresponding projection points p_i $(i = 1 \sim 10)$. The coloured arrows above the figure, matching the light paths, indicate the positional variations of these projection points. The stretch ratio of the zebra stripes is defined as:

$$\eta_i = \frac{\overparen{p_i \rightarrow p_{i+1}}}{\overparen{r_i \rightarrow r_{i+1}}}, \, i = 1 \sim 9, \tag{3.2}$$

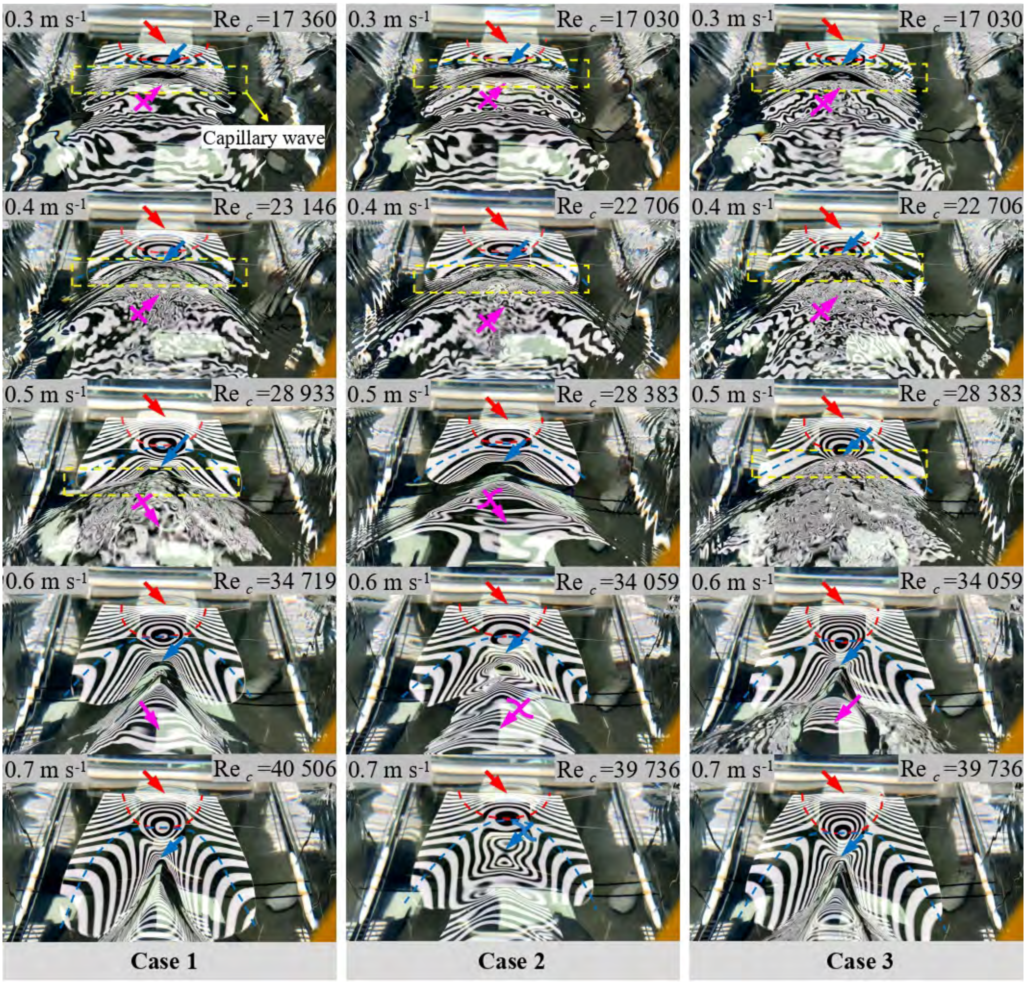

Figure 9. Zebra stripe patterns for Cases 1 to 3.

where η_i reflects the average stretch ratio between points p_i and p_{i+1}. Evidently, $\lim_{p_i \to p_{i+1}} \eta_i$ can represent the local stretch ratio. Considering that p_i may exhibit turning points at t_1 and t_2, '$\rightarrow$' is used here to distinguish the displacement between these two points from the conventional arc length. When η_i is greater than 1, the pattern on the free surface is compressed, resulting in denser stripes; conversely, it is stretched when η_i is less than 1. The degree of compression or stretching is proportional to the magnitude of η_i.

For the reflection points in figure 8, η_1 at p_1 (bulge wave) reaches its maximum and decreases during the transition from $p_1 \rightarrow p_3$. The stripes are most densely concentrated over the head wave peak. Near p_3, a topological change in the stripes begins (i.e., the inverse process at $t_1 \rightarrow t_2$), accompanied by a thickening of the stripes. When a gradient in curvature exists along the spanwise direction (typically with curvature decreasing away from the deformation core on both sides), the LED panel stripes reflected from the central plane of the model generally appear further downstream. Thus, the topological pattern manifests as concentric rings. In figure 8, the projection points $p_3 \rightarrow p_7$, corresponding to reflection points $r_3 \rightarrow r_7$, reverse direction and point upstream until the end of t_2 in the arrow diagram. Thereafter, projection points beyond r_7 ($p_7 \rightarrow p_{10}$) consistently move

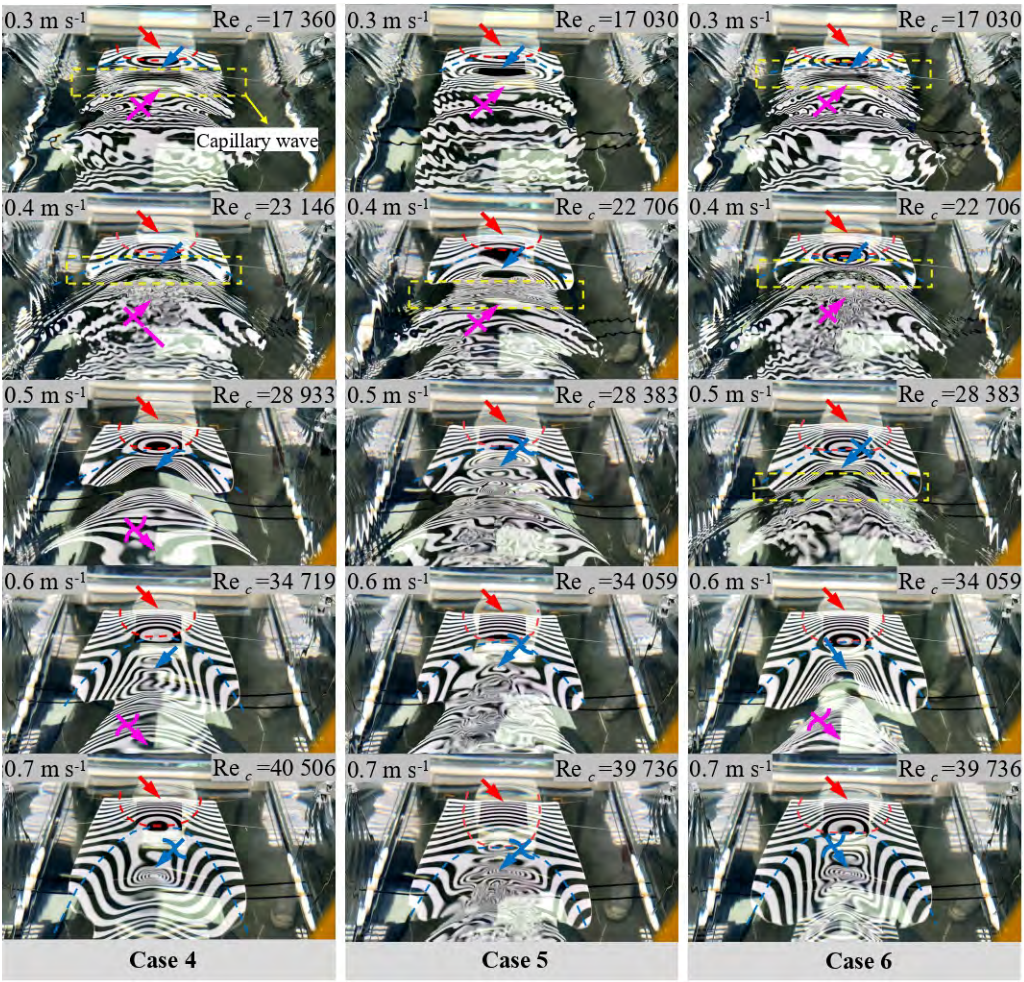

Figure 10. Zebra stripe patterns for Cases 4 to 6.

downstream, indicating that only regions downstream of r_7 in the camera view will exhibit reflective stripes with conventional distribution.

Observing p_3 to p_7, one can find $\eta_5 = Max\,\{\eta_3, \eta_4, \eta_5, \eta_6\}$. The compressive effect can be used to identify the location of the trough at r_5, where the stripes are locally most dense and close to the downstream position of the first topological concentric ring. Similarly, the decrease in stretch ratio as the projection points move toward p_{10} implies gradually widening stripes near the wake wave peak. It should be noted that the turning point t_2 in figure 8 lies outside the LED panel, indicating possible discontinuities between upstream and downstream stripes. This phenomenon is related to the curvature of the wave trough. If the depression at r_5 is shallow and the range of $\overparen{p_3 \rightarrow p_7}$ is small enough such that t_2 falls within the LED panel, the stripe pattern remains continuous despite the topological transition. Based on the principles described above, the approximate extent and peak location of the bugle wave are indicated by red dashed lines and arrows. The approximate starting boundary and trough of the depression wave are marked with blue dashed lines and arrows. The approximate peak location of the wake bulge wave is indicated by magenta

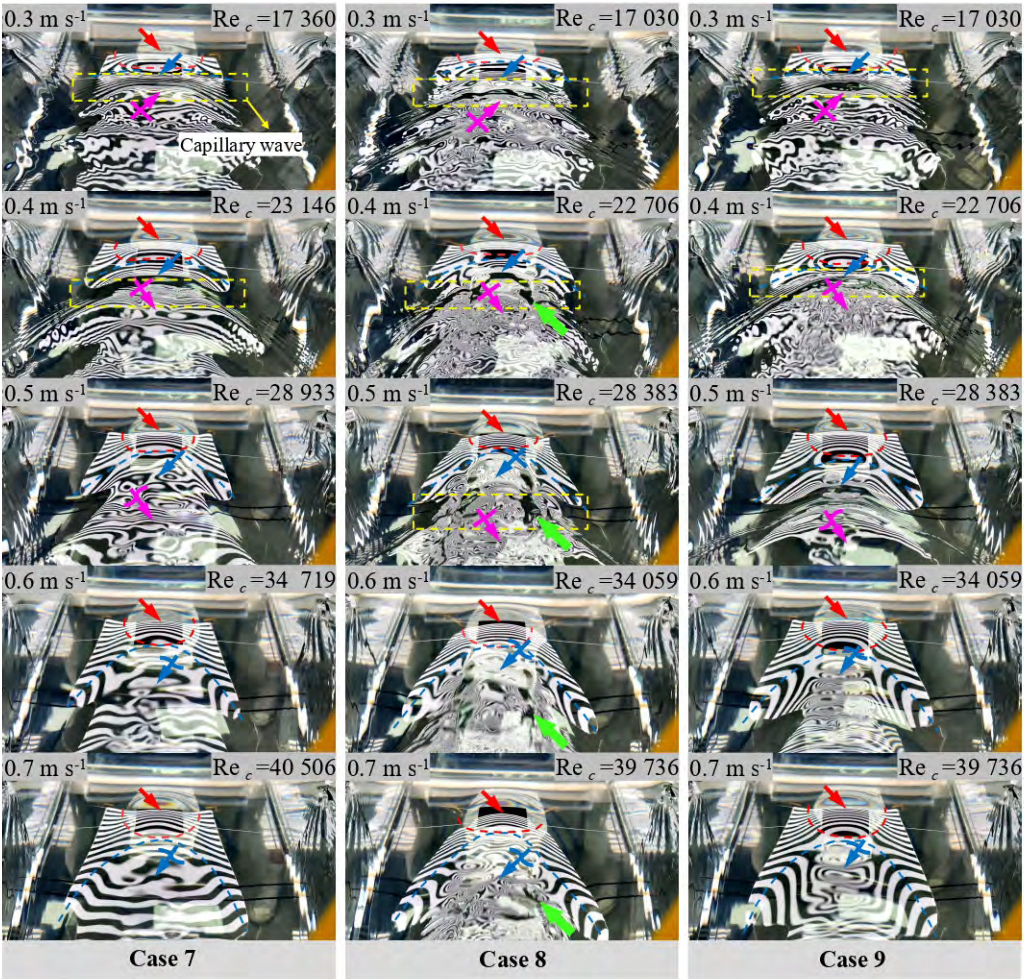

Figure 11. Zebra stripe patterns for Cases 7 to 9. The dark fringes indicated by the green arrows are traces of the model tip vortices striking the water surface (Zhang *et al.* 2020).

arrows. The absence of any annotation implies that no valid physical information can be identified.

The waves depicted in figures 9 to 11 exhibit three-dimensional characteristics. A small convex bulge typically forms above the model, while a concave bow wave develops at the model's stern, representing a specific derivative of Kelvin wave patterns under the given operational conditions(Xue *et al.* 2020). At low towing speeds (< 0.4 to $0.5\mathrm{m\ s^{-1}}$), capillary waves are observed on the upward slope plane downstream of the trough (within the yellow dashed box). The liquid surface exhibits low steepness, and capillary waves display only localized instabilities. The wavelength of capillary waves decreases toward the center of the wave trough, where they are densely packed, while the wavelength gradually increases toward the outer flanks. The waves fan outward, and this spanwise variation arises from differences in the crest velocity and trough velocity of the capillary waves in the spanwise direction (Duncan *et al.* 1999). Outside the capillary wave region, the surface generally remains calm, except for faint vortex impingement traces immediately downstream of the depression wave—specifically in the region of maximum surface curvature—where a

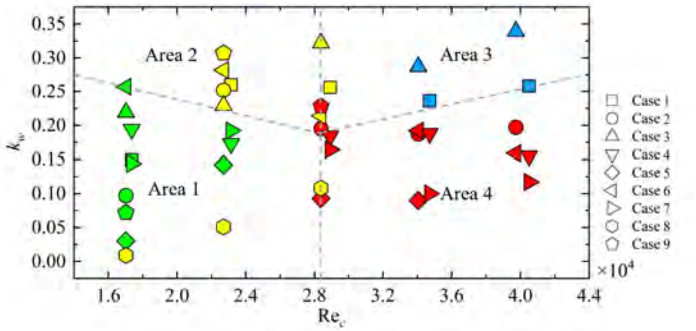

Figure 12. Distribution of wake types under different k_w (slopes of the line connecting wave crests and troughs) and towing speeds, where Type 1 to 4 wakes are represented by green, yellow, blue, and red respectively.

locally sharpened fine annular topological pattern emerges. As the towing speed increases continuously, this local vorticity rapidly diffuses and destabilizes, evolving into large-scale breaking waves that cover the entire area enclosed by the Kelvin wave pattern. A key transition occurs when the towing speed increases beyond a certain threshold (approximately 0.5 to 0.6m s^{-1}): the capillary waves disappear. At this point, the vorticity near the interface downstream of the trough undergoes a complete transformation, leading to a flow state dominated either by large-scale vortices or a smooth, steady interface. According to the study of Longuet-Higgins (1992), the initial stage of short gravity wave breaking involves the appearance of parasitic capillaries. As the Reynolds number increases further, gravity induces a natural downward sliding of the interface along the sloped water surface behind the trough (Duncan *et al.* 1994). This sliding fluid impacts the leeward face of the wave; the intervening fluid is continuously entrained, forming a shear layer. Separation from the underlying fluid triggers a turbulent state, leading to the formation of a capillary roller (Longuet-Higgins 1992). Dimas & Triantafyllou (1994) indicated that intense horizontal shear is the primary trigger for small, sharp surface waves near the free surface at low Froude numbers. Interestingly, he capillary waves were absent in Case 5 at the lowest Reynolds number. Observation of figure 6 reveals that the trough depth for Case 5 is shallow. A flatter wave surface is less prone to interface breaking. Deike *et al.* (2015) previously noted that waves with low initial steepness remain stable, propagating smoothly without breaking. When the trough steepness is small, capillary waves induce only localized interfacial vorticity near the trough.

Typically, vortices shed from the orca stern impinge on the water surface downstream of the wave trough (downstream of the blue arrow). However, in Case 8, vortex impingement is observed upstream of the capillary wave. Figure 11 presents snapshots of the interfacial vortex structures for Case 8 at different Reynolds numbers. At the lowest Reynolds number, evidence of large-scale vortex impingement is observed at the upstream trough location relative to the capillary waves, while the area downstream of the capillary waves shows dense, small striations formed by the impingement of small-scale, high-frequency waves. When the Reynolds number increases to 28 383, the impingement of large-scale structures even makes the wave trough difficult to discern. As the Reynolds number increases further, the wake becomes dominated by large-scale structures and the capillary waves disappear gradually. The upward flow-guiding tendency of Case 8 is highly evident, as it convects the tip vortices from both sides of the model to the vicinity of the interface, where their impingement on the free surface leaves visible ‘traces’, as indicated by the green arrows

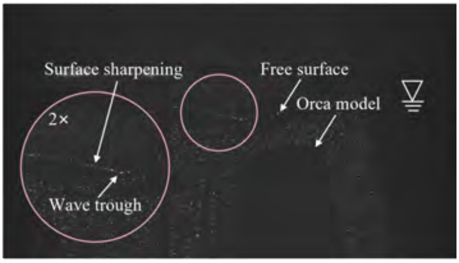

Figure 13. A snapshot of the deformed water surface for Case 3 at a towing speed of 0.3 m s^{-1}.

in the figure. The development path of vortices downstream of an irregular cross-section body is closely related to its attitude (Subburaj *et al.* 2018), a point that will be discussed in Section 3.2 regarding the underwater flow structures. The subsequent part of this section continues to focus on the characteristics of vortex impingement on the interface.

Based on the morphological differences of the impinging vortices, the model wake is categorized into four types. Type 1 features small-scale shedding vortex structures that cause small-range vortex impingement on the surface. The diameter of a single vortex is much less than W_m. These vortices shed from the wave trough and collide with the deformed surface, with an emergence width of one to several times the diameter of the impact vortex, which subsequently diminishes or vanishes as they follow the wake. Type 2 involves wide-range small-scale vortex structures. When the Reynolds number further increases on the basis of the Type 1 wake, shortly after the formation of the depression, the wake instantly transitions into a large-area ‘orange peel’ pattern covering the entire downstream region of the depressed wave that induces large-area intensive fluctuations in the wake region. The initial width is significantly larger than W_m, and its extent is confined within the band-like depression region (the region downstream delineated by capillary waves). The vortex impingement frequency is higher than in Type 1. Individual vortex sizes are at the level of Type 1 and are distributed very densely. Type 3 forms a steady wake region where the surface is smooth, the streak spacing is highly regular, and the curvature variation is small. No action between the shedding vortices and the liquid surface is observed. This scenario typically occurs in cases with deeper tail depression waves. Type 4 involves large-scale shedding vortex structures, where the size of a single vortex is often comparable to Wm. These structures gradually enlarge while developing downstream. Adjacent vortex structures usually appear sequentially without clustering, which may be related to the spanwise asymmetry of the vortex structures. Study showed that this characteristic is one cause of the aperiodic nature of vortex shedding and is a feature of wakes behind finite-aspect-ratio models, with asymmetric flows more prone to occur at higher Reynolds numbers (Taira & Colonius 2009). In figures 9 to 11, a slash bar ‘$\diagdown$’ added to an arrow indicates small-scale vortex structures, a wavy line ‘$\sim$’ denotes large-scale vortex structures, and the absence of a symbol represents steady flow. If an arrow lacks an annotation, it implies that the flow feature at that location is difficult to identify, for instance, if it is outside the field of view.

Deike *et al.* (2015) indicated that the Bond number and the initial wave steepness can be used to classify wave regimes, as surface tension significantly influences interfacial wave development. We propose that the wake type is associated with both the Reynolds number and the steepness of the wave concavity. We have plotted the wake type, Reynolds number, and the downslope steepness k_w (defined in figure 8) in a single diagram. When the wave depression is limited and the towing speed is low, Type 1 wake dominates and is distributed in Area 1. Capillary waves downstream of the wave trough are typically observed in this

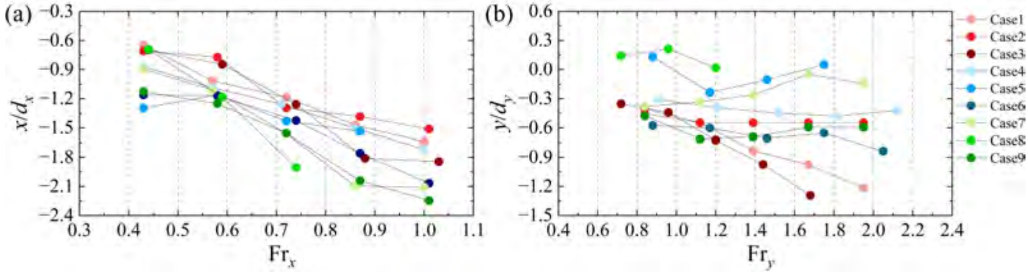

Figure 14. (a)

regime. Case 8 unexpectedly appears in this region because its attitude forcibly guides the trailing vortices toward the surface. As k_w increases, the wake transitions from Type 1 to Type 2. The spatial extent of Type 2 wake is considerably larger than that of Type 1, and their underlying formation mechanisms differ. The steeper slope promotes the formation of a jet beneath the trough and a large-scale mixing layer near the free surface, generating numerous surface vortices, Lin & Rockwell (1995) investigated wave breaking phenomena downstream of a hydrofoil and observed that with increasing Froude number, capillary waves are replaced by large-scale free-surface distortions, which are induced by flow separation near the free surface at the wave trough where the radius of curvature is large. Figure 13 displays a wave profile for Case 3 at the lowest towing speed, in which the trough and the subsequent upslope exhibit sharpening. As the flow velocity increases, the sharpened trough becomes more prone to intense flow separation. When both the depression depth and the velocity are relatively high, the wake transitions from Type 2 to Type 3. In this case, the capillary waves behind the trough disappear, and severe curvature variations on the interface are significantly reduced. The free surface in Type 3 is smooth, indicating a steady flow state, and no vortex impingement is observed within the camera's field of view. It is worth noting that Type 3 may require a specific deeper wave trough. In most cases where a sufficiently deep concave wave cannot be formed, the wake exhibits patterns left by the impingement of large-scale vortices, that is, the Type 4 wake. We tend to believe that Type 3 and Type 4 are essentially the same underwater flow pattern, i.e., strouhal vortex shedding state, with the distinction lying in whether the large-scale wake vortices are convected to shallower surface-sensitive regions.

It is evident that the initial state of the liquid surface corresponds to Type 1. As the wave trough deepens and its curvature increases, flow shear instability beneath the trough triggers a transition to Type 2. With a further rise in the Reynolds number, capillary waves disappear, and stable flow at the trough replaces flow separation. If the wake intensity is high or its position is close to the water surface, the large-scale vortex structures will reach the interface, leading to a transition to Type 4. Conversely, if the wake intensity is weak or is guided by the model to deeper layers, it becomes insufficient to affect the interface, resulting in a transition to Type 3. The presence of capillary waves serves as a critical indicator of the transition from Type 1/2 to Type 3/4, corresponding to a Reynolds number range of 28 000 to 29 000.

At low Froude numbers, the free surface can stabilize the flow field, while high Froude numbers typically induce large-amplitude waves. The Froude number is closely related to the stability of the downstream wake (Triantafyllou & Dimas 1989). Some studies indicated that at low Froude numbers, the interaction between vortices and the free surface resembles that with a rigid surface, whereas at high Froude numbers, significant deformations occur (Yu & Tryggvason 1990; Tryggvason *et al.* 1991). Although free-surface deformations

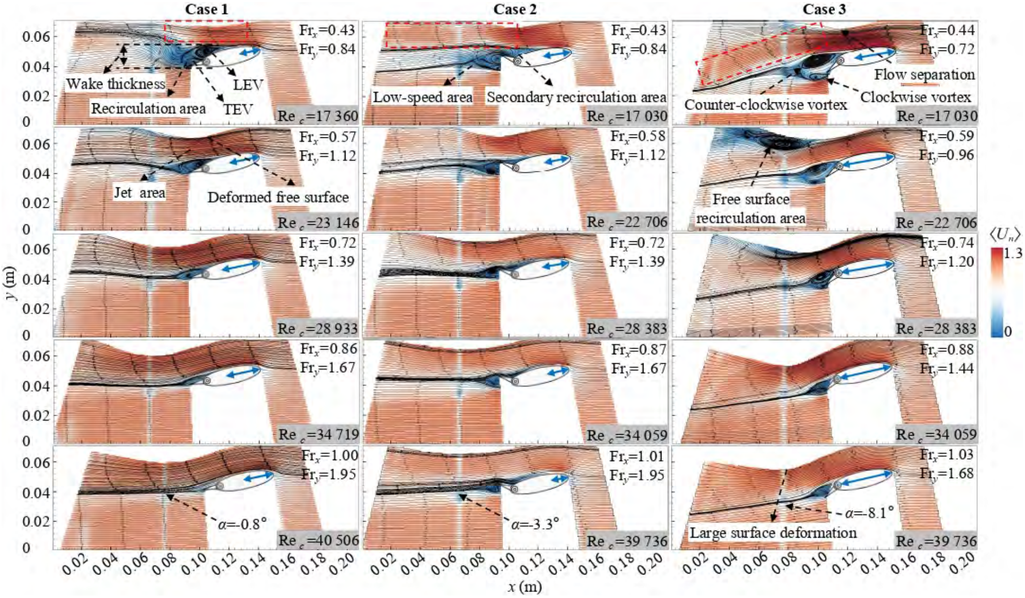

Figure 15. Time-averaged velocity for Cases 1 to 3 at different Reynolds numbers.

induced by near-surface cylinders have been extensively studied (Sheridan *et al.* 1995, 1997; Reichl *et al.* 2005; Sun *et al.* 2025), the Froude number for a cylinder is determined solely by its diameter. In contrast, the present model involves two distinct Froude numbers: the streamwise Froude number Fr_x and the normal Froude number Fr_y. The dimensionless depth and streamwise position of the trough of the depression wave are plotted against the corresponding directional Froude numbers in figure 14. For all cases, as Fr_x and Fr_y increase, the wave trough moves farther away from the orca model. However, the depth of the trough is influenced by the model's attitude. Several differences are noteworthy. Regarding the streamwise position x/d_x, the trough in Cases 1 to 3 remains closer to the model, with a moderate rate of change as Fr_x increases. In contrast, cases 7 to 9 exhibit a more pronounced downstream shift with increasing Fr_x. Although data for Case 8 is incomplete, its trend suggests a substantial displacement, and based on the results in figure 6, it can be anticipated that the trough will appear further downstream. In comparison, Cses 4 to 6 show lower sensitivity to Fr_x, with x/d_x being the least responsive to changes in Fr_x.

Regarding the dimensionless trough depth y/d_y, Cases 1 and 3 show a rapid deepening of the trough with increasing Fr_y, resulting in significant depression waves at high Froude numbers. Case 6 exhibits a similar trend but at a reduced rate. The remaining cases show minimal change in y/d_y with increasing Fr_y. For complex models, the trend of free surface variation cannot be evaluated solely by the Froude number, as the contribution of the geometry of the flow-disturbing cross-section may be comparable to that of the Froude number. The study by Daichin & Lee (2004) indicated that even for elliptical cylinders with aspect ratios of 3 to 4, the influence of surface curvature on free surface deformation and wake flow structure exceeds that of the Froude number. Given the greater complexity of the model in this study, the influence of the Froude number is likely to be less significant than in traditional bluff bodies. The interaction mechanism between the vortex structures behind the orca model and the free surface is complex and requires further analysis of the flow field below the water surface.

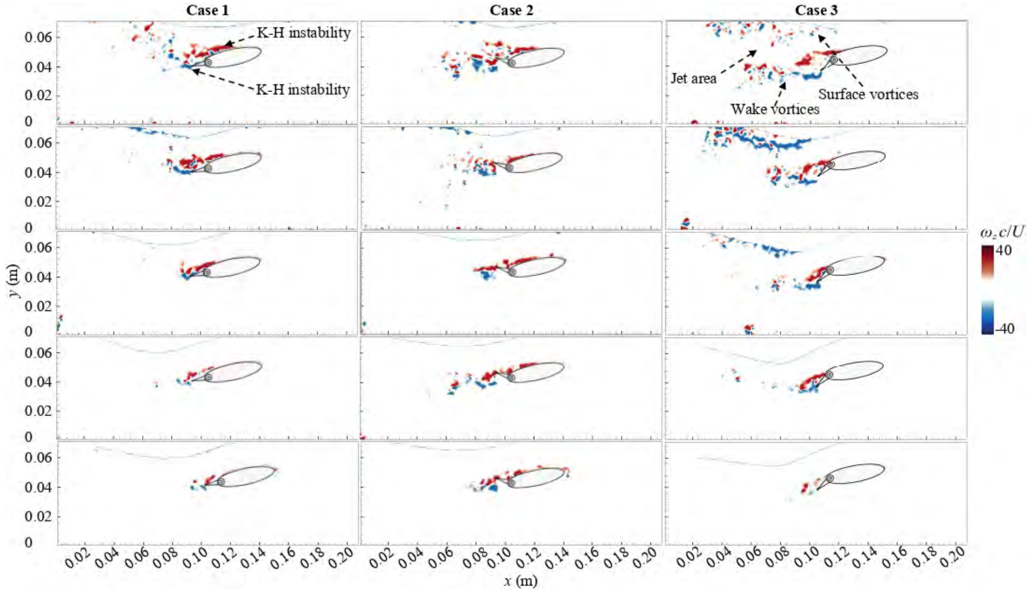

Figure 16. Instantaneous vorticity for Cases 1 to 3 at different towing speeds.

3.2. *Flow field below the water surface*

The geometric shape features an elliptical cross-section with major and minor axes in approximately a 4:1 ratio. The model has two free ends and will be installed at a pitching angle of attack in some cases. Additionally, a rudder is attached to the downstream trailing edge, which can flip upward or downward along the spanwise axis. When towed beneath the free surface, the model satisfies both asymmetric boundary conditions and asymmetric geometric conditions (Inoue & Sakuragi 2008; Subburaj *et al.* 2018; Samsam-Khayani & Seyed-Aghazadeh 2025). The asymmetric boundary conditions arise from the combined effects of the geometry and the free surface. Unlike the periodic wake patterns typically observed under symmetric boundary conditions, the wake flow structure of the orca model is expected to undergo significant alterations due to additional constraints (Taneda 1965; Alzabari *et al.* 2023). The asymmetric wake induced by the angle of attack was initially investigated by Fage & Johansen (1927). Primary focus is often placed on boundary layer development, subsequent shear layer instability, and the separation of leading- and trailing-edge vortices, phenomena that have been extensively analyzed in studies of flow around flat plates (Perry & Steiner 1987; Nakamura *et al.* 1991; Samsam-Khayani & Seyed-Aghazadeh 2025). This section examines the flow dynamics around the orca model in different attitudes using time-averaged velocity fields, time-averaged vorticity fields, time-averaged swirling strength vector fields, instantaneous vorticity, and streamlines.

The dimensionless vorticity $\omega_{z,n}$ is obtained by normalizing the vorticity $\omega_z = \partial v/\partial x - \partial u/\partial y$ using the chord length c and the towing speed U_∞:

$$\omega_{z,n} = \frac{\omega_z c}{U_\infty}, \tag{3.3}$$

The time-averaged dimensionless vorticity $\langle \omega_{z,n} \rangle$ characterizes the average distribution of vorticity over time in the wake of the model. The coherent-structure identification criterion based on λ_{ci} is employed to detect and characterize vortex structures in complex flow fields. This method is grounded in the concept of swirling strength and involves

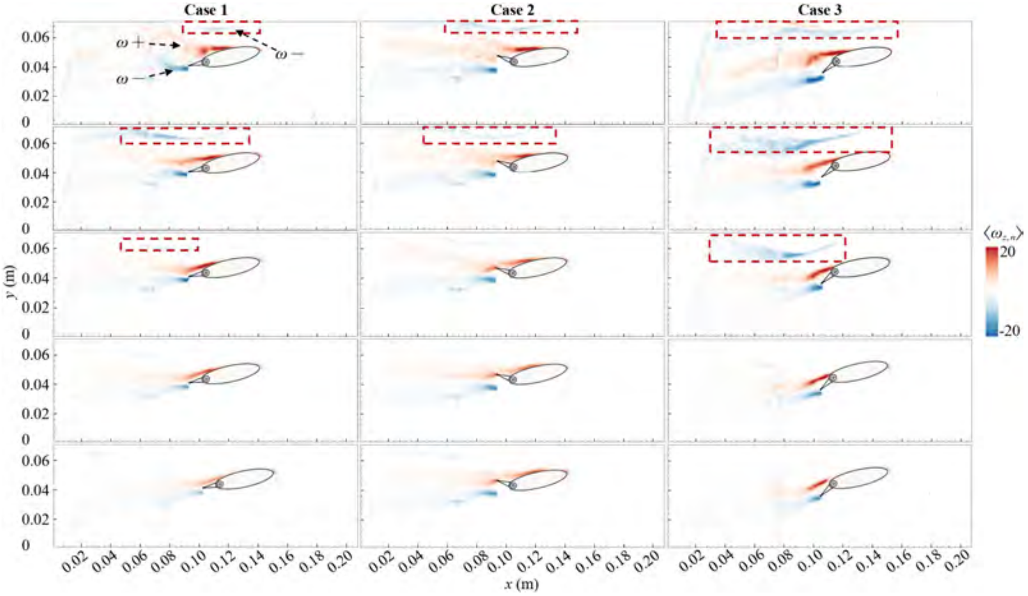

Figure 17. Time-averaged vorticity for Cases 1 to 3 at different towing speeds. The red dashed box marks the negative vorticity diffusing into the water from the wave trough.

analyzing the eigenvalues of the velocity gradient tensor **eig** (∇**u**). Regions with enhanced vortex activity are identified by the presence of a complex eigenvalue pair, with higher λ_{ci} values indicating stronger swirling motion and highlighting the presence of coherent vortices (Zhou *et al.* 1999; Haller 2005). Samsam-Khayani & Seyed-Aghazadeh (2025) applied this approach to analyze vortex shedding from an inclined plate near a free surface. A vortex is identified by a complex eigenvalue pair of the velocity gradient tensor, representing rotational motion within a defined plane. The swirling strength is defined as follows:

$$\lambda_{ci} = \mathrm{Im}\left(\mathbf{eig}\left(\nabla\mathbf{u}\right)\right) = \mathrm{Im}\left(\mathbf{eig}\begin{bmatrix}\dfrac{\partial u}{\partial x} & \dfrac{\partial u}{\partial y}\\ \dfrac{\partial v}{\partial x} & \dfrac{\partial v}{\partial y}\end{bmatrix}\right), \tag{3.4}$$

swirling strength is non-dimensionalized using the chord length c and the towing speed U_∞:

$$\lambda_{ci,n} = \frac{\lambda_{ci}c}{U_\infty}. \tag{3.5}$$

Its time-averaged value $\left\langle\lambda_{ci,n}\right\rangle$ can simultaneously characterize both the time-averaged distribution of vortex strength in the flow field and the development trajectory of coherent structures.

Figures 15 to 18 present the time-averaged velocity (with streamlines), instantaneous vorticity, time-averaged vorticity, and time-averaged swirling strength for Cases 1 to 3 at different Reynolds numbers. When the model is at an angle of attack, shear layers of varying strength and size form at the leading and trailing edges, causing an imbalance in the wake (Nakamura *et al.* 1991). For Case 1, at the lowest Reynolds number (Re_c = 17 360), an accelerated jet forms at the model's leading edge, undergoes laminar separation a short

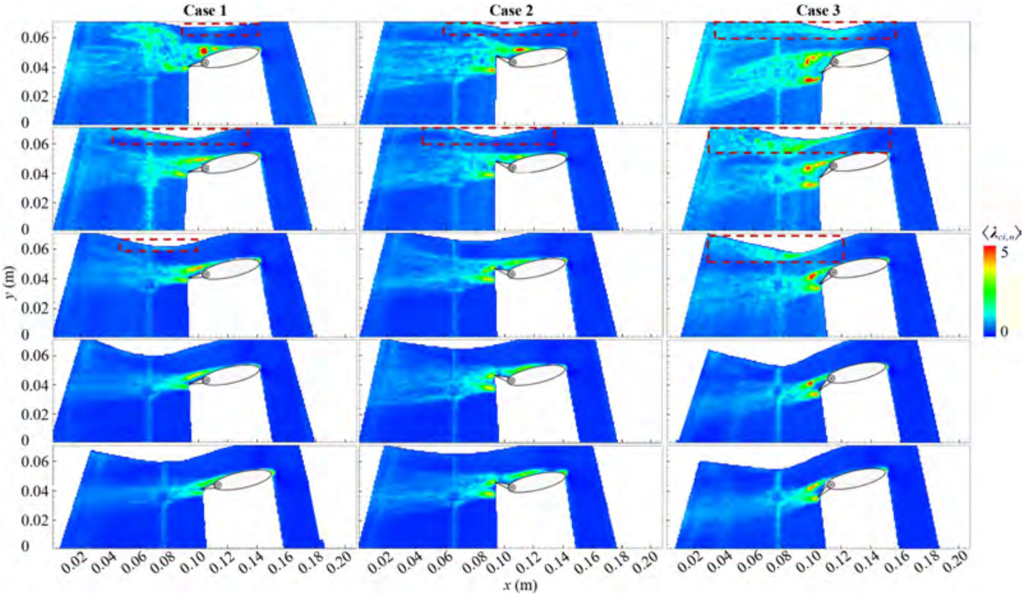

Figure 18. Time-averaged swirling strength for Cases 1 to 3 at different towing speeds. The red dashed box marks the active vortex activity caused by surface wave breaking.

distance downstream, and generates a counterclockwise leading-edge vortex (LEV) on the model's suction side. A clockwise trailing-edge vortex (TEV) forms above the tail fin, and the positions of these two vortices show significant asymmetry, together constituting a large-scale, low-velocity recirculation area. In case 1, the low-velocity recirculation area remains attached to the model's dorsal surface. As the Reynolds number increases, the recirculation area compresses towards downstream, the wake thickness decreases, and the asymmetric dual vortex ring structure degenerates into a single vortex ring before eventually disappearing.

Generally, the edges of the vortex ring produce strong shear, and the separated shear layer undergoes Kelvin-Helmholtz (K-H) instability, forming numerous irregular small-scale vortical structures, see figure 16. As the flow interacts and merges with the large-scale recirculation vortex ring. According to experimental results from Lin *et al.* (1995), K-H small-scale vortices are the core feature of the instantaneous flow in the present Reynolds number range. These small-scale structures are embedded within the large-scale structure, forming a complex wake topology. In Case 1, the LEV attached to the model's back impedes the attachment of the jet to the surface at the lowest Reynolds number ($\mathrm{Re}_c = 17\,360$). As the boundary layer separates, the jet detaches from the model surface and deflects upward along the edge of the recirculation area. The deformed free surface then exerts an 'elastic'-like constraint on the jet (Barker & Crow 1977), causing it to deflect again downstream beneath the free surface, with its strength significantly weakened. The high-speed flow beneath the model wraps around the edge of the low-velocity recirculation area, entraining fluid to compensate for the wake. The asymmetric instability of the vortex ring causes the low-velocity fluid to deflect and diffuse toward the free surface. Studies on the wake of upward-inclined hydrofoils by Taira & Colonius (2009) indicate that after the leading-edge vortex separates, its position elevates away from the model surface, consistent with the observations in this study. The separated wake structure displaces to approximately $0.5d_x$

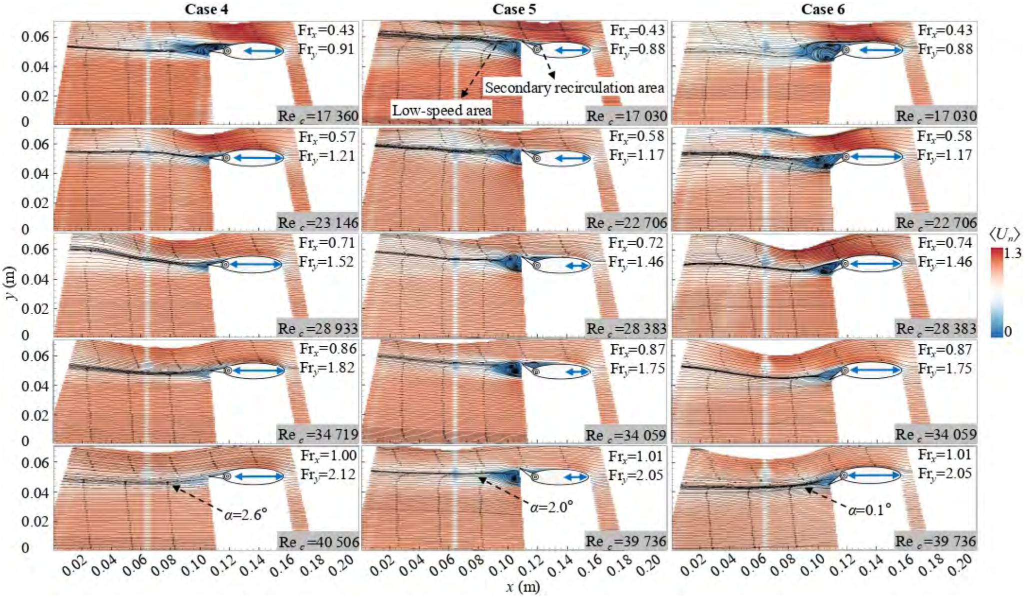

Figure 19. Time-averaged velocity fields for Cases 4 to 6 at different Reynolds numbers.

downstream of the model below the water surface and interacts with it. Figure 18 illustrates the diffusion path of the vortex structure within the recirculation area.

As the Reynolds number increases, the recirculation area compresses, reducing its obstruction to the jet. The reattachment length L_a of the jet (refer to the blue double-headed arrow) initially increases and then decreases, reaching its maximum ($L_a = 26.59$ mm, $L_a/c = 0.53$) at $\mathrm{Re}_c = 28\,933$. Below this Reynolds number, the increase in reattachment length ($L_a = 14.6\mathrm{mm} \rightarrow 26.59\mathrm{mm}$) is dominated by the increased dynamic pressure in the flow field above the stagnation point at the model's leading edge. Above this Reynolds number, the subsequent decrease in reattachment length ($L_a = 26.59$ mm $\rightarrow 21.06$ mm) is caused by the increased cross-flow kinetic energy between the leading edge and the free surface, leading to flow detachment from the surface and suppressing the Coandă effect (Samsam-Khayani & Seyed-Aghazadeh 2025). The jet attached to the model's back can guide the wake to deflect downward, increasing the degree of free surface deformation. When the $\mathrm{Re}_c > 28\,933$, the jet streamlines and the deformed free surface exhibit synchronized curvature, as if the jet is adhering to the deformed surface. At lower Reynolds numbers, localized negative vorticity ($\omega-$) diffusing from the surface into the fluid interior can be observed at the wave trough locations, as circled by the red dashed box in figure 17. When $\mathrm{Re}_c > 28\,933$, this localized negative vorticity at the trough disappears. Correspondingly, figure 9 shows that the capillary waves also vanish, and the downstream wake interface becomes smooth. The instantaneous vorticity and swirling strength results indicate that, at this stage, the jet hinders the contact between the model's trailing vortices and the interface, and the jet area is almost devoid of vortical structures.

In Case 2, influenced by the raised tail fin, the separated vortex ring is located downstream of the fin, exhibiting better symmetry compared to Case 1. A small-scale, low-velocity secondary recirculation area forms in the region enclosed by the model's back and the raised tail fin. This low-velocity region persists across all tested towing speeds in Case 2 and connects with the low-velocity region in the wake. As the Reynolds number increases, the secondary recirculation area extends upstream, while the reattachment length of the jet

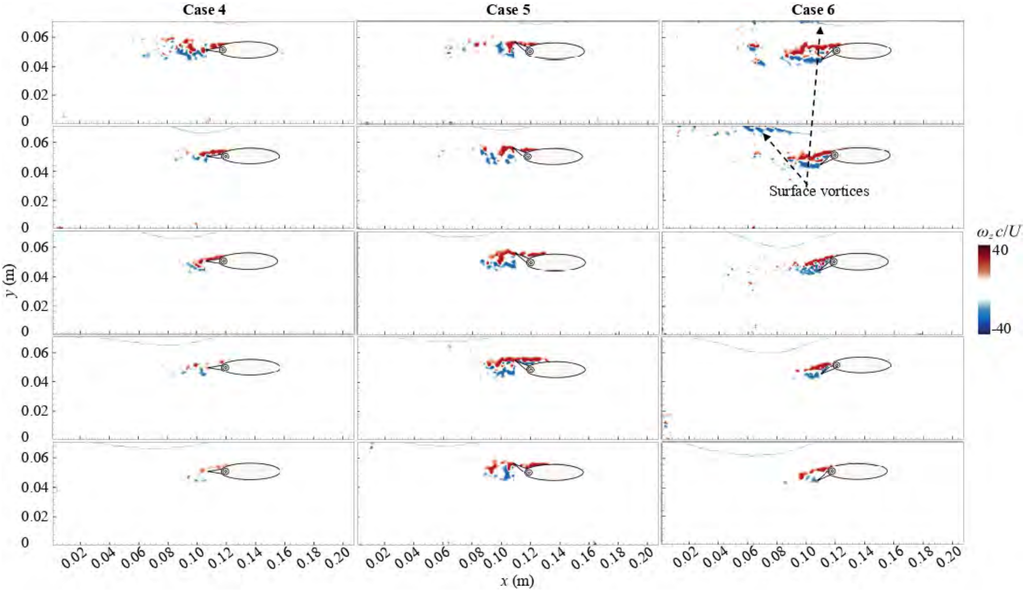

Figure 20. Instantaneous vorticity for Cases 4 to 6 at different towing speeds.

continues to shorten (L_a = 19.81 mm → 12.98 mm), leading to earlier flow separation. Both the secondary recirculation area and the vorticity near the tail fin exhibit positive vorticity (ω+), and they dominate the shedding of trailing vortices. Since the primary recirculation area is confined below the tail fin, the jet passes over the fin tip without a block. Compared to Case 1, the more symmetric trailing vortex ring balances the wake, resulting in smoother streamlines. However, the low-velocity wake region in Case 2 is thicker than in Case 1, and the squeezing effect of the jet on the wake is weak. It is hypothesized that the extended low-velocity region along the model's back weakens the kinetic energy of the jet. This hypothesis is supported by the subsequent results; the time-averaged velocity profiles behind the model show that the minimum velocity in the wake recirculation area and the maximum velocity in the jet area of Case 2 is both lower than in Case 1, especially at higher Reynolds numbers ($Re_c \geqslant 28\,383$). Another effect of the raised fin is that it elevates the trailing vortices, which is associated with substantial shedding of positive vorticity at the higher fin tip. The continuous region of positive vorticity (ω+) intensifies this effect. When $Re_c > 34\,059$, large-scale vortex impingement occurs on the free surface, classified as a Type 4 wake, induced by the large-scale Strouhal vortices shedding from the tail. When these large-scale structures convect near the interface, they cause pressure fluctuations, forming localized surface elevations. In Case 2, due to the effect of attitude, the shed vortices do not propagate into deeper water regions, and their trajectories exhibit a roughly horizontal motion pattern (refer to the streamline angle α in figure 15). The jet does not completely isolate the large-scale vortices from the surface, which may be attributed to its own weakened state and the greater thickness of the wake in Case 2 (see figure 18).

In contrast, the downward-folded tail fin in Case 3 leads to markedly different outcomes. The trailing vortex ring in Case 3 is almost entirely located downstream of the model. The absence of a secondary recirculation area on the model's back eliminates any obstruction to jet attachment, allowing the jet's reattachment length to increase continuously with rising Reynolds number (L_a = 28.18 mm → 36.11 mm). When $Re_c > 22\,706$, the jet nearly

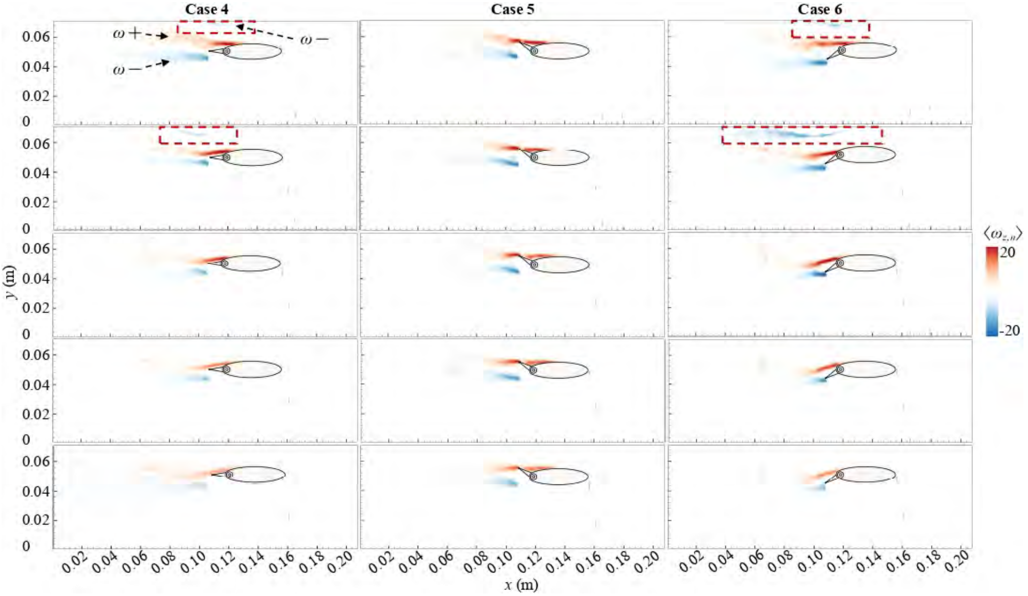

Figure 21. Time-averaged vorticity for Cases 4 to 6 at different towing speeds. The red dashed box marks the negative vorticity diffusing into the water from the wave trough.

completely covers the model's upper surface. At higher Reynolds numbers, inertial forces dominate over viscous forces, promoting flow attachment to the wall (Samsam-Khayani & Seyed-Aghazadeh 2025). The thickness of the low-velocity wake region decreases as the Reynolds number increases, and the symmetric vortex ring is progressively compressed into a single, small vortex core.

At the lowest Reynolds number ($\mathrm{Re}_c = 17\,030$), the downstream part of the low-velocity recirculation area closes rapidly. After closure, the streamlines form an angle ($\alpha \approx -8.1^\circ$) with the incoming flow, intensifying the jet's pulling effect on the free surface. This angled wake streamline pattern is a common feature in Case 3. Time-sequence animations of the instantaneous vorticity field (not shown in the paper) reveal that large-scale vortex structures are carried deeper into the flow by the jet. The jet's deflection triggers interfacial instability on the downstream slope of the wave trough. The severe separation between the jet and the overlying low-velocity fluid at the trough location leads to a more pronounced transition to wave breaking further downstream, generating a more extensive breaking region than in Cases 1 and 2. The vorticity being convected originates from the amplification of disturbances within the mixing layer formed by prior flow separation. The initiation point of the shear layer rests at the trough of the deformed surface, i.e., the location of maximum curvature, consistent with the analysis in Section 3.1.

For $\mathrm{Re}_c = 22\,706$ and $28\,383$, a counterclockwise recirculation area appears downstream of the wave trough. Multiple vortex lines are observed terminating at the deformed surface, indicating intense energy exchange. The termination of streamlines at the free surface is a key indicator of the vortex region's visibility (Samsam-Khayani & Seyed-Aghazadeh 2025). 16 and 17 show that free-surface breaking at this stage generates a large area of negative vorticity, which diffuses downstream from the wave trough (red dashed box in figure 17). In contrast, the swirling strength figure indicates that vorticity levels near the free surface remain relatively low. Research by Lin & Rockwell (1995) suggests that the maximum circulation values for Type 1 and Type 2 small-scale breaking waves are of the

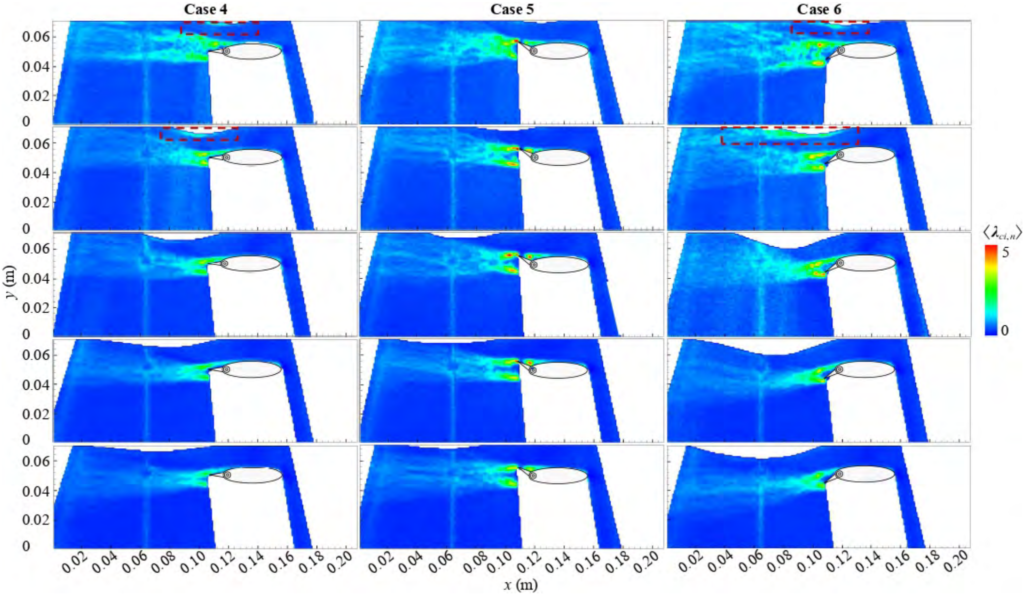

Figure 22. Time-averaged swirling strength for Cases 4 to 6 at different towing speeds. The red dashed box marks the active vortex activity caused by surface wave breaking.

same order of magnitude. The jet above the model acts as a barrier, separating the negative vorticity from the free surface and the positive vorticity from the model's upper surface. Within the viewing range, these two regions do not interact, thus preventing crossover and mutual annihilation.

The study of Shen *et al.* (1999) shows that surface vorticity is generated by the zero tangential stress condition at the free surface. The development and trajectory of vortices, as well as their evolution with other vortices, are influenced by the interface morphology and surface tension (Ohring & Lugt 1991). The conclusions of Terrington *et al.* (2022) indicate that both the normal velocity and curvature of the free surface increase with the Froude number, leading to the generation of more significant secondary vorticity at the free surface, which is consistent with the observed results. Reichl *et al.* (2005) studied the flow disturbance near a surface-piercing cylinder, where the downstream jet caused significant curvature changes in the depression wave, resulting in the generation of counter-signed shedding vortices on the upper surface. Different from the present study, the jet in their work could not sufficiently isolate these vortices from interacting with the shedding structures in the wake; therefore, they rapidly diffused away from the free surface and underwent crossover and annihilation with the large-scale wake vortices downstream. Numerous studies on bluff body disturbances near the air-water interface have documented vortex breaking and vorticity aggregation phenomena induced by depression waves (Lin & Rockwell 1995; Duncan & Dimas 1996; Iafrati & Campana 2005; Longo *et al.* 2014; Brøns *et al.* 2014; Bouscasse *et al.* 2017; Subburaj *et al.* 2018; Karmakar & Saha 2020; Jin *et al.* 2021; Zhao *et al.* 2022; Guo *et al.* 2023; Alzabari *et al.* 2023; Alzabari 2025; Sun *et al.* 2025). The numerical study by Patel *et al.* (2025) also observed the entrainment of micro-bubbles into the wake, noting that the absence of interface deformation or rupture can suppress the generation of interfacial vorticity. Recently, Samsam-Khayani & Seyed-Aghazadeh (2025) documented capillary waves generated downstream of a deformed free surface behind an inclined plate, accompanied by the generation of secondary vortices

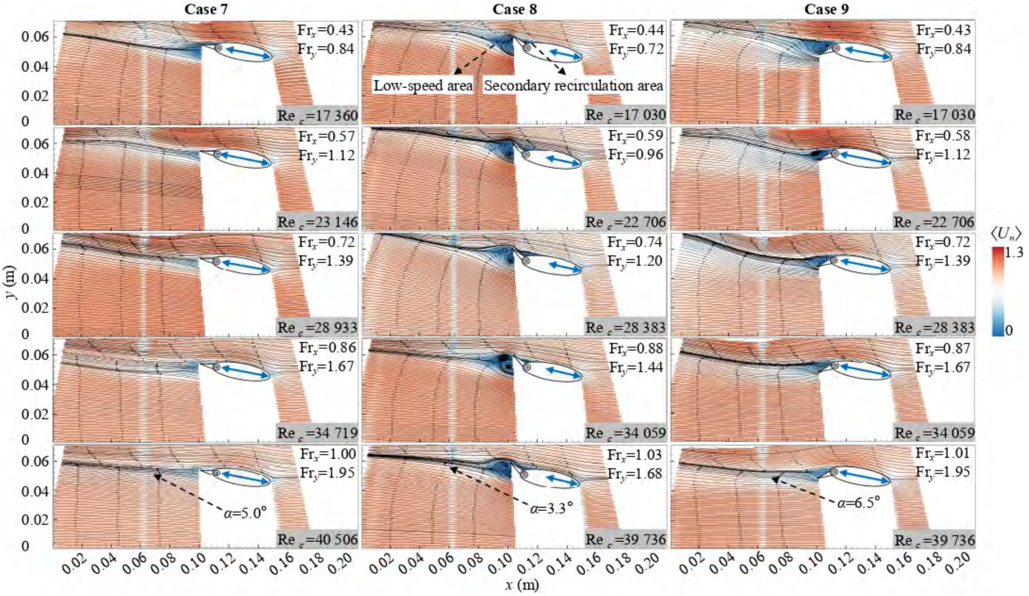

Figure 23. Time-averaged velocity fields for Cases 7 to 9 at different Reynolds numbers.

beneath the free surface and wavy shear mixing layers, which resemble the observations in this study. At the high Reynolds numbers, the free surface undergoes more extensive deformation. Influenced by the Coandă effect, the jet can undergo secondary attachment, adhering to the deformed free surface. At this stage, the free surface recirculation area disappears, and the negative vorticity associated with wave breaking is no longer visible. Figure 18 clearly record the sudden disappearance of active coherent vortex structures near the water surface.

The K-H instability near the wave trough perfectly corresponds to the small-scale turbulent patterns recorded in figure 9. The presence of this instability correlates with observable wave breaking at the water surface, indicating that the small-scale turbulent structures on the surface are induced by interfacial K-H instability. Small-area wave breaking is only observed at low Reynolds numbers associated with small-amplitude depression waves, suggesting that the minor deformation (both in extent and depth) at the center of the depression wave cannot induce wave breaking far from its center. The vorticity is concentrated within a thin layer near the interface. Research by Deike *et al.* (2015) indicates that vorticity is generated at both the troughs and crests of capillary waves. This result demonstrates universality, as vorticity typically emerges from regions of high interfacial curvature (Lugt 1987; Lugt & Ohring 1992). These observations are not unique to Case 3. A cross-comparison of the vorticity fields for Cases 1 and 2 reveals that localized negative vorticity is generated at the trough of the depression wave in Case 1 at Re_c = 17 360, 23 146, and 28 933; and in Case 2 at Re_c = 17 030 and 22 706. Swirling strength plots provide corroborating evidence. Cross-referencing with figure 9 shows that capillary waves appear on the water surface, accompanied by downstream small-scale wave breaking. Furthermore, observation of the vorticity fields reveals that when the jet reattachment length is short, the vorticity intensity associated with the shear layer in the model wake decays rapidly. Conversely, in Case 3, the jet boundary is not weakened by a low-velocity recirculation area, resulting in a more pronounced Coandă effect. Consequently, the wake shear layer maintains a high shear intensity. Figure 16

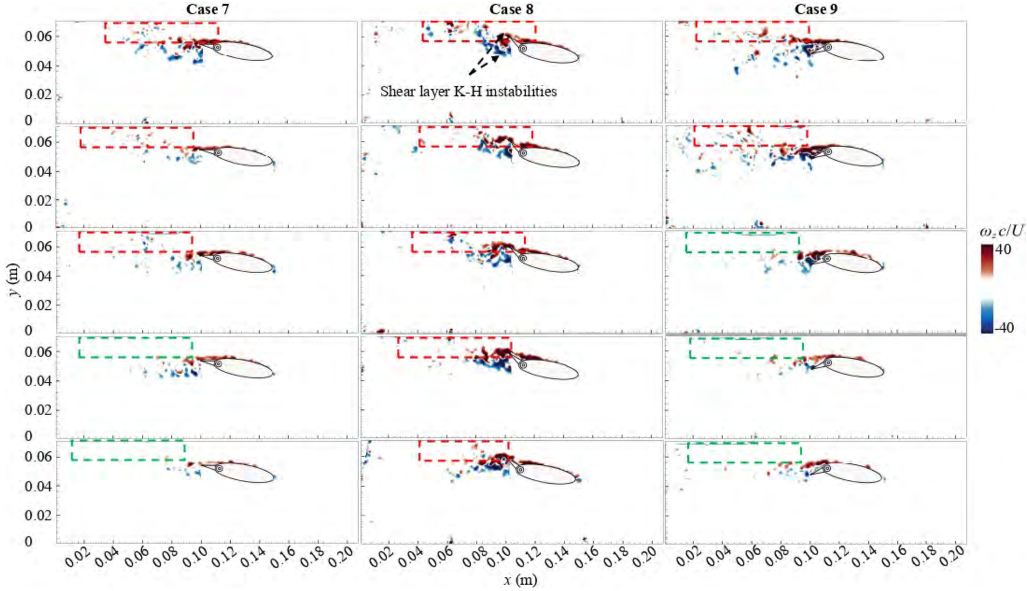

Figure 24. Instantaneous vorticity for Cases 7 to 9 at different towing speeds. The red dashed box marks the diffusion of dense small-scale vortex structures toward the interface, while the green dashed box shows no significant diffusion of small-scale vortices.

further indicates that the jet exerts a compressing and constraining effect on the diffusion of the trailing vortices, but it has little effect on altering the positions of the active vortex cores within the wake under convective action (highlighted regions). These positions reflect the active trajectories of periodic coherent structures.

When a jet approaches an inclined or curved surface, the Coandă effect can cause the fluid to adhere to and develop along the solid wall. Viscous forces promote jet attachment to the wall, while inertial forces drive the jet along its original path. Their combined action can cause the jet to deviate from its expected trajectory. Wall morphology can guide and constrain fluid flow. This effect, induced by fluid viscosity, is governed by multiple factors, including flow velocity, curvature, position, and boundary conditions (Ahmed 2019). Given that this effect can alter the flow field around an object, when a disturbance-generating object approaches a free surface, the deformed free surface constitutes a second, different attachable surface distinct from the solid wall. The curved deformed surface, shed vortices, and the flow around the body can form a more complex interaction mechanism. Sheridan *et al.* (1997) documented the critical state of trailing vortices induced by the brief attachment of a jet to a free surface. Hoyt & Sellin (2000) reproduced the experiments of Sheridan *et al.* (1997), observing various jet attachment phenomena in experiments with different submergence depths. Carberry (2002) recorded three wake modes for a cylinder approaching a free surface, one of which involved flow attachment to the free surface. The presence of a deformable free surface introduces an asymmetric boundary condition, thereby influencing wake shedding. Non-ideal jet attachment can lead to free surface deformation, thereby causing the formation of surface vorticity (Sheridan *et al.* 1995; Reichl *et al.* 2005; Sareen *et al.* 2018; Cleaver *et al.* 2013). Shallow submergence depth is likely a key factor enabling jet attachment. Research by Chen & Chwang (2002) suggests that the jet on the upper surface of a hydrofoil with a higher submergence ratio is not as pronounced as observed in studies like Sheridan *et al.* (1997). Samsam-Khayani & Seyed-Aghazadeh (2025) argue that the free surface further constrains and guides the

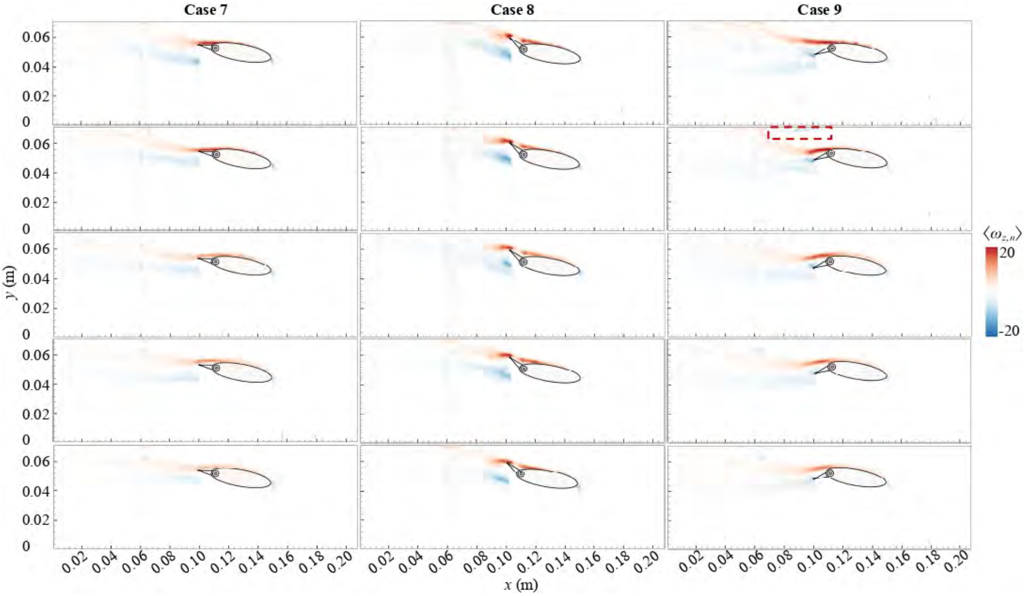

Figure 25. Time-averaged vorticity for Cases 7 to 9 at different towing speeds. The red dashed box marks the negative vorticity diffusing into the water from the wave trough.

flow over a plate via the Coandă effect. The second Coandă regime (CII) mentioned in their work involves the jet being compressed by larger free-surface deformation, thereby increasing the attachment length covering the plate's leading edge.

Observing figures 16 and 17, it is evident that at high Reynolds numbers, the jets in Case 3 transport large-scale vortex structures into deeper water flow, reducing the impact of trailing vortices on the interface. This is the reason for the smooth interface of the Type 3 wake. In the present study, the large trailing depression wave in Case 3, together with the curved back surface of the model, forms an ideal jet channel. The stable and robust jet enhances the stability of the depression wave. This large-scale depression wave and associated jet attachment have never been observed in cylinder-induced disturbances. The upward-tilted head and downward-swept tail behavior in Case 3 is the posture we observed and consider optimal for the killer whale's ice-breaking during hunting. The large, smooth depression wake generated by Case 3, devoid of interfacial wave breaking, implies that interfacial energy is not dissipated, leaving significant surface potential energy within the system (Deike *et al.* 2015). Zhao *et al.* (2021) suggests that fluctuations in both the jet velocity component and hydrodynamic forces are suppressed. This sets the stage for efficiently utilizing the depression wave to manipulate and subsequently break ice.

Figures 19 to 22 present the time-averaged flow fields, instantaneous vorticity, time-averaged vorticity fields, and time-averaged swirling strength fields for Cases 4 to 6 at different Reynolds numbers. When the model body angle is 0°, the model's blocking effect on the flow field is weakest. For Case 4, a recirculation area attached to the upper surface of the tail fin is only observed at the lowest Reynolds number. As the Reynolds number increases, this recirculation area is compressed and degenerates, with the low-velocity region located directly behind the model. The reattachment length of the upper-surface jet is very weak, showing an initial increase followed by a decrease. The depth of the depression wave also exhibits a trend of first increasing and then decreasing. For Cases 5 and 6, the downstream recirculation vortex ring consistently appears on the side opposite

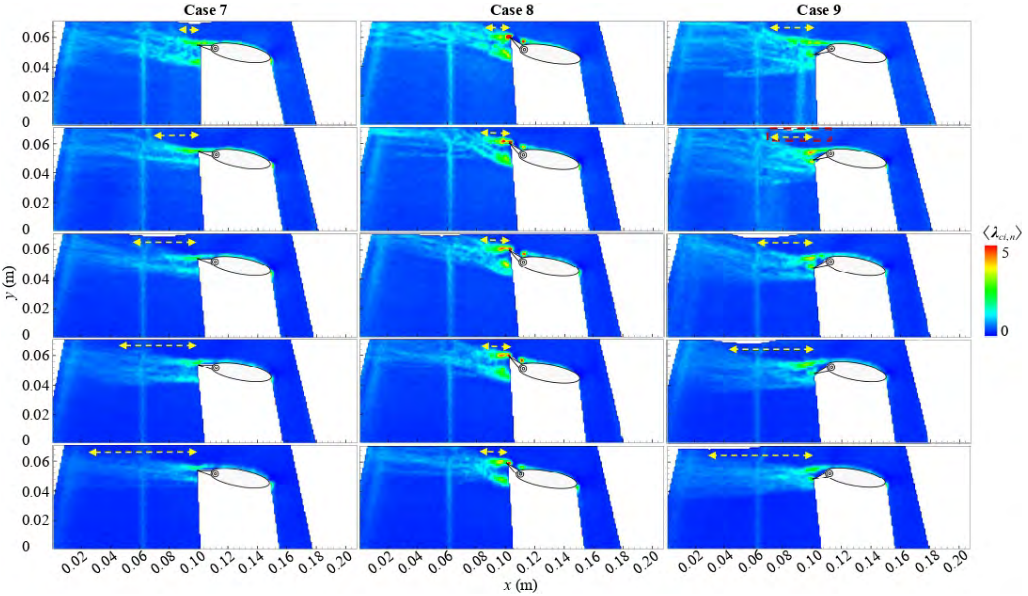

Figure 26. Time-averaged swirling strength for Cases 7 to 9 at different towing speeds. The yellow arrows in the figure mark the extension length of the jets.

to the direction of the fin's flip, near its back. The sharp fin tip induces strong flow separation, leading to the aggregation of high vorticity (see figures 20 and 21) and the formation of a larger downstream recirculation area. In Case 5, the secondary recirculation area and the wake recirculation area remain connected, forming a longer low-velocity boundary. The displacement effect of the secondary recirculation area also leads to a shorter jet wall-attachment effect. In contrast, Case 6 experiences less flow interference on its back. The jet separation point is located further downstream, and when $\mathrm{Re}_c > 22\,706$, the jet can completely attach to the surface of the model's back. Consequently, Case 6 can generate a stronger back-jet with a larger outflow angle, thereby inducing greater free-surface deformation. A cross-comparison of the relationship between depression wave depth and reattachment length for Cases 4 to 6 reveals a positive correlation; the reattachment capability of the back jet likely determines the degree of wake depression. This is corroborated by the lateral comparison of Cases 1-3 before. Due to the suppression of the depression wave, although capillary wave breaking occurs in Case 5 (at towing speeds of 0.4 m s^{-1}), the trough depression is insufficient to generate concentrated vorticity, which is not effectively identified in figures 21 and 22. The vorticity induced by capillary waves is related to the jet strength, free-surface curvature, and local capillary wave intensity under specific operating conditions.

When the model body is at a negative angle, the trailing depression wave is significantly suppressed, which is related to the flow above the model being forced towards the free surface. Figure 23 presents the wake streamlines for Cases 7 to 9, all showing an upward inclination. This angle is larger at moderate Reynolds numbers and smaller at low or high Reynolds numbers. Benefiting from the effect of a favorable pressure gradient in the incoming flow, the jet reattachment lengths in Cases 7 and 9 are close to the model body length. Nevertheless, the flow directed towards the water surface cannot stretch the free surface and cause large-scale deformation like a downward-impinging jet. It is also observed that jet development is impeded by both the low-velocity region near the tail and the free surface, leading to a significant reduction in jet intensity. Interestingly, in figure 11, Case 7 forms a Type 1 wake at low Reynolds numbers. When the $\mathrm{Re}_c > 34\,719$, the pattern transitions to large-scale periodic vortex shedding. Considering that concentrated negative vorticity never appears at the depression wave location, the small-scale impinging vortices are likely induced by K-H shear vortices at the edge of the recirculation zone. They diffuse and impinge on the free surface due to entrainment by the jet. The instantaneous vorticity field shows the diffusion of these small-scale vortex structures beneath the free surface. The development length of the dorsal jet increases significantly (yellow arrow in figure 26). However, except for the velocity above the model's highest point still exceeding the towing speed, a distinct and consistent jet is no longer apparent. At this stage, large-scale vortex structures in the wake dominate, eventually disturbing the free surface to form a Type 4 wake.

For Case 8, intense laminar separation occurs at the tip of the upward-flipped tail fin. The shear action generates numerous small-scale K-H vortex structures. Given that Case 8 has the smallest relative submergence depth (h/d_y), these vortex structures shedding from the fin tip are more prone to interact with the surface. The zebra-stripe results show that the interaction between vortex structures and the free surface in Case 8 is very active. Ring-like topological patterns from impingement even appear upstream of the wave trough, and large areas of small-scale impinging vortices exist downstream at all Reynolds numbers, with a width $> W_m$. Referring to figure 26, the short jet development length causes the entrained vortex structures to impinge on the free surface before significant dissipation. According to the instantaneous vorticity field, a multitude of K-H shear vortices are transported near the free surface, a feature clearly captured in the figure(see the red dashed box). Although the flow above the model is still referred to as a 'jet', in Case 8 it accelerates only above the tail fin tip, with no acceleration over the main back surface of the model, making the term 'jet' somewhat tenuous. It is important to note that when $\mathrm{Re}_c \leqslant 28\ 383$, capillary waves can be observed behind the wave trough. These capillary waves disappear as the Reynolds number further increases. This suggests that for $\mathrm{Re}_c \leqslant 28\ 383$, the interface might originally have been a Type 1 or Type 2 wake, depending on the depression wave depth, but the fin's flow-guiding action forced a conversion to the current Type 2 wake. This also explains why the wake type for Case 8 in figure 12 appears in the Area 1 region.

In contrast, when the tail fin is flipped downward (Case 9), the jet can be stretched, having a relatively larger extension space, forming the deepest depression wave among Cases 7 to 9. When $\mathrm{Re}_c = 22\ 706$, negative vorticity is generated beneath the free surface at the wave trough (red dashed boxes in figures 25 and 26), corresponding to the Type 2 wake in figure 11. As the Reynolds number increases further, it transitions to a Type 4 wake.

Figure 27 presents the non-dimensional time-averaged velocity profiles along the vertical height, taken approximately $1/5d_x$ downstream of the model's trailing edge. The recirculation zone induced by the separation of the sharpened wave trough at the free surface causes the profile to exhibit an inverted 'S' shape. The jet immediately adjacent to the free surface leads to local curves in the upper right subplot exceeding the critical value of $U/U\infty = 1$ (black dashed line). The dual-vortex ring structure within the low-velocity region behind the model results in an 'M'-shaped double-peak profile, whereas a single peak indicates a single vortex ring in the wake. Case 3 and Case 8 exhibit the deepest and shallowest low-velocity wake regions, respectively, which is related to the jet ejection angle. Case 3 forms the most distinct and thickest jet across all towing speeds. In contrast, the jet in Case 8 is almost degenerate, with its velocity even lower than the freestream velocity. In Case 3, the most pronounced jet occurs at 0.6 m s^{-1}, while the maximum wave trough depth appears at 0.7 m s^{-1}. The Case 3 configuration demonstrates the strongest

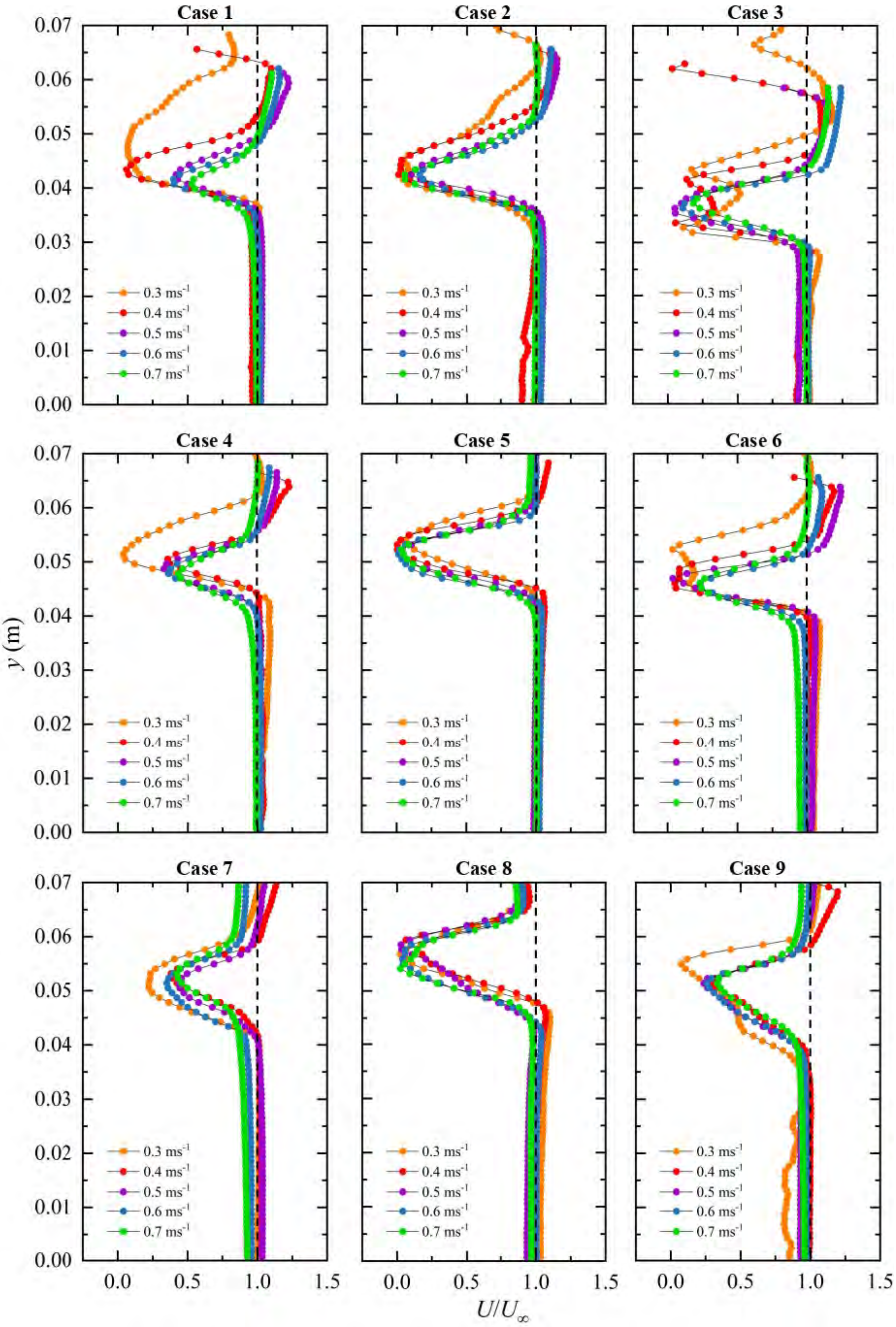

Figure 27. Mean velocity profiles in vertical direction.

capability to maintain both a low-velocity region and a developed jet. In the region below the mixing layer, the velocity profiles tend to converge into a single curve; fluctuations in individual curves at greater depths are caused by errors from laser sheet refraction at the deformed surface.

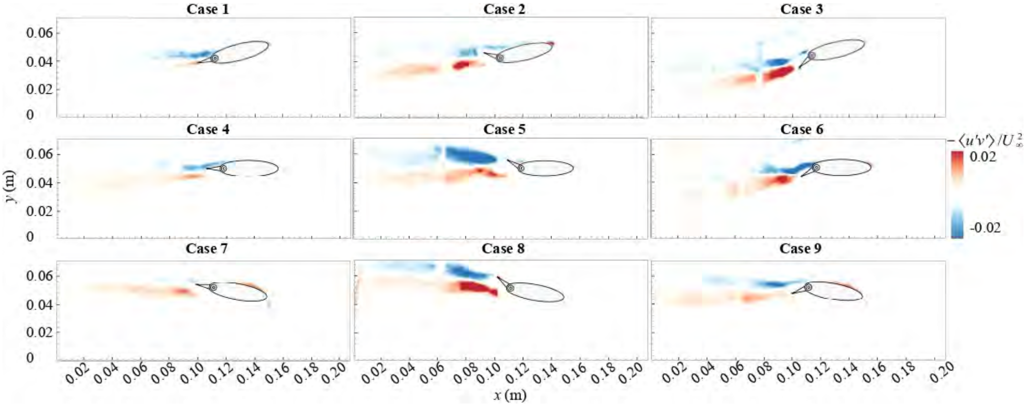

Figure 28. Distribution of time-averaged Reynolds stress for each case at the towing speed of 0.7 m s^{-1}.

Figure 28 displays the Reynolds stress distribution beneath each configuration at the maximum towing speed, revealing locations of the most intense turbulent momentum exchange in the model's wake. It can be observed that when the tail fin angle is 0°(Cases 1, 4, and 7), the interface resembles a hydrofoil with smooth surface curvature, leading to weaker turbulent activity and stable, well-ordered flow fields on both the upper and lower surfaces. When the raised tail fin interacts with the jet (Cases 5 and 8), localized acceleration and intense shear separation occur at the fin tip, generating high-intensity, extensive areas of negative Reynolds stress. This indicates more vigorous vortex structure oscillation and shedding. Corresponding positive Reynolds stress forms beneath the model, signifying unstable separated flow. The tip stress in Case 8 is weaker than in Case 5, which is associated with the weaker back-jet in Case 8. In Case 2, the low-velocity area extending continuously from the secondary recirculation region to the wake envelops the tail fin tip. Some vortex structures separated from the model's leading edge merge directly with the trailing vortices. The separation at the fin tip is mitigated by the low-velocity area, resulting in a corresponding decrease in Reynolds stress. In Cases 3, 6, and 9, the flow separation at the tail fin tip remains strong, but its intensity and extent are less than in Cases 5, and 8. When the tail fin is submerged within the turbulent wake without forming direct shear with the incoming flow, the region immediately behind the fin shows lower Reynolds stress, potentially leading to lower flow resistance and a reduced model blockage effect. Furthermore, the jet influences the transport of Reynolds stress. Readers are encouraged to compare the turbulence level in the zebra-stripe patterns in figure 9 to 11 at the maximum towing speed with the magnitude and spatial distribution of the Reynolds stress. It will be apparent that Reynolds stress directly affects the level of interfacial turbulence. As it is currently not feasible to quantitatively assess the turbulence intensity from the zebra-stripe images, a direct data comparison on this aspect is not performed in this study.

3.3. *Wave-induced ice breaking*

A moving free-surface depression wave can generate disturbances on floating objects. We first selected a large, continuous ice floe as the study object and conducted experiments for different cases at towing speeds ranging from 0.3 to 0.7 ms^{-1}, performing 15 independent tests at each speed. Before the experiments, the ice floe model was carefully positioned on the water surface, with the spanwise center plane of the floe aligned with the spanwise symmetry plane of the orca model. Since the ice floe remained unconstrained during the experiments, it could drift during towing. To ensure result accuracy, the 10 most ideal

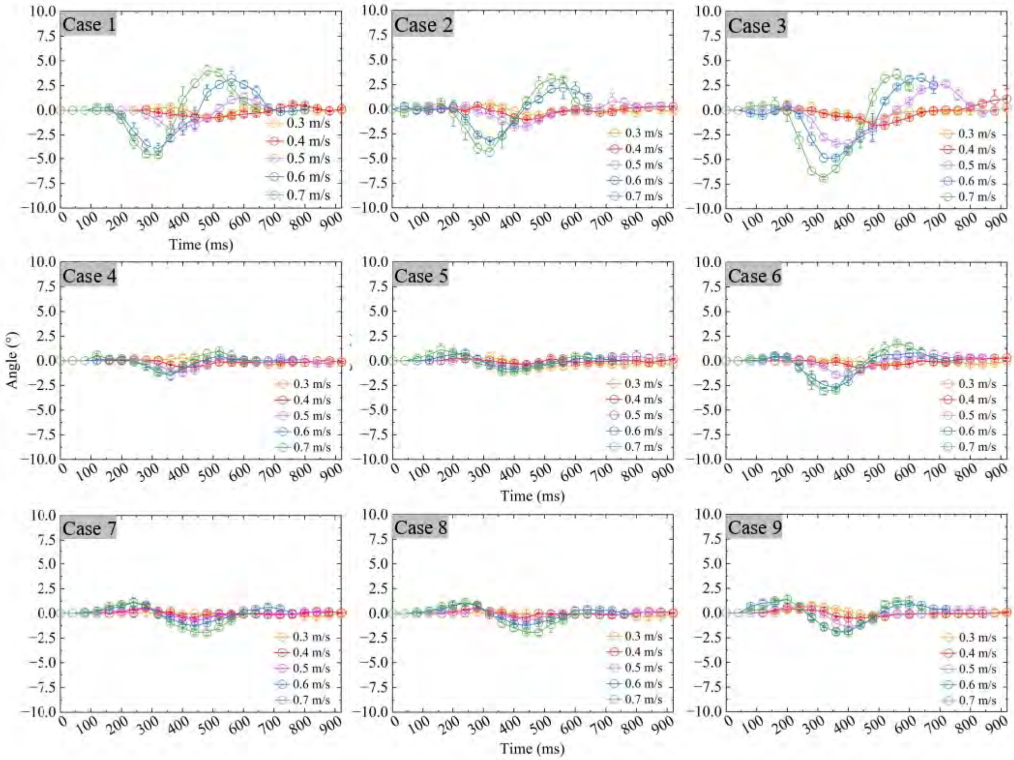

Figure 29. The variation of the tilt angle α_T of large ice floes over time. The results were obtained by averaging 10 independent measurements, with error bars representing the standard deviation of the statistical results. The tilt angle becomes negative as it tilts downward from the horizontal towards the wave trough.

outcomes were ultimately selected. Additionally, in some cases, the depression waves caused the ice floe model to fracture; such exceptional results were excluded. The time-varying curves of the ice floe tilt angle are shown in figure 29. Across different postures, higher swimming speeds tended to produce more pronounced ice floe tilting. Specifically, Case 3 at 0.7 ms^{-1} generated the largest tilt angle, approximately $-6.9°$, whereas Case 5 exhibited the least significant tilting effect, with a tilt angle of only $-1.1°$ at 0.7 ms^{-1}. A comparison with figure 6 indicates that the downslope gradient k_w of the depression wave influenced the tilting potential of the ice floe, and a deeper depression wave led to a more significant tilt angle. It should be noted that the tilt angle of the large ice floe was significantly smaller than the inclination angle of the depression wave's downslope surface.

Following the conclusion in the previous section, the posture with the head oriented downward and the tail raised tends to generate a hydraulic jump, forming a convex wave above the model. The ice floe initially compresses the convex wave, causing an upward tilt, and then flips downward into the trough of the depression wave after passing over the convex wave. If the body posture remains unchanged, flipping the tail fin downward tends to generate a more pronounced depression wave. In figure 30, we present snapshots of the interaction between the ice floe and Cases 3, 6, and 9. The development time relative to the first snapshot is labeled in the figure. In all three cases, the ice floe reaches its maximum tilt angle at approximately +160 ms after the depression wave reaches the edge of the ice floe. In Case 9, the impact between the ice floe and the convex wave near the head is

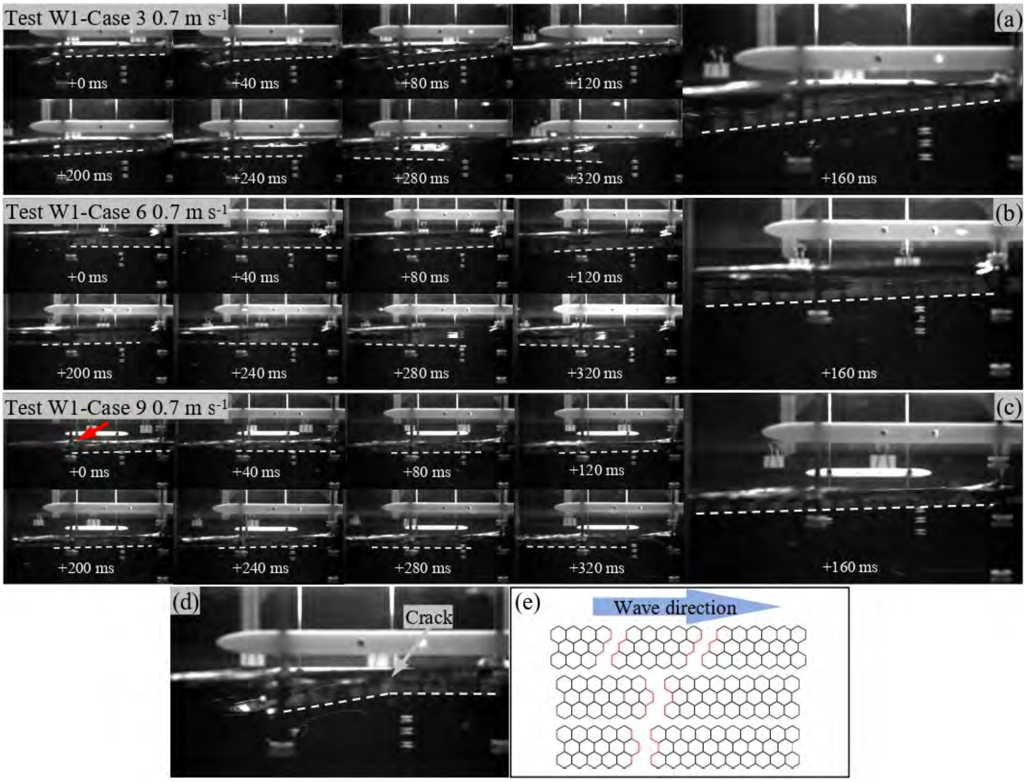

Figure 30. Tilting effect of depression waves on the large ice floe model at maximum towing speed. The figure presents a snapshot of one selected set of experimental results. Subfigure (a), (b), and (c) correspond to Cases 3, 6, and 9, respectively. The dashed lines in the images indicate the inclined state of the ice floe model in each frame. (d) shows the moment when the leading edge of a large ice floe enters the depression wave and subsequently fractures. (e) illustrates the distribution of fracture cracks in a large ice floe induced by the trailing depression wave in Case 3.

observed (indicated by the red arrow). The ice floe first tilts slightly upward (1.4°) and then flips downward into the wave trough (−2°), which is consistent with the statistical results in figure 29. The impact of the convex wave appears to have no significant effect on the subsequent behavior of the ice floe. Among all the results, fracture of the ice floe only occurred at the highest towing speed in Case 3, when the leading edge of the large ice floe moved above the trough of the depression wave. Figure 30(d) shows a snapshot of the moment of fracture. Out of all 15 experiments, fracture occurred only three times, and the locations of the three sets of cracks are shown in figure 30(e). If the ice floe is simplified as a rectangular plate with finite thickness, neglecting the effects of viscous forces in water and the inertial forces of the ice floe on ice breaking, the buoyancy of the overhanging portion decreases sharply when it moves above the depression wave. The moment induced by the gravity of the overhanging part will cause the ice floe to tilt. The bending stress generated at the front end of the ice floe due to its own weight can be expressed as:

$$\sigma_b = \frac{M\left(x\right) \cdot 0.5H_{im} \cdot \cos\left(\alpha_T\right)}{I_z}, \tag{3.6}$$

among them, $M\left(x\right)$ is the moment of the overhanging portion of the ice floe, $0.5H_{im}$ is the half-thickness of the ice floe, and $\cos\left(\alpha_T\right)$ is the tilt angle coefficient, which is related

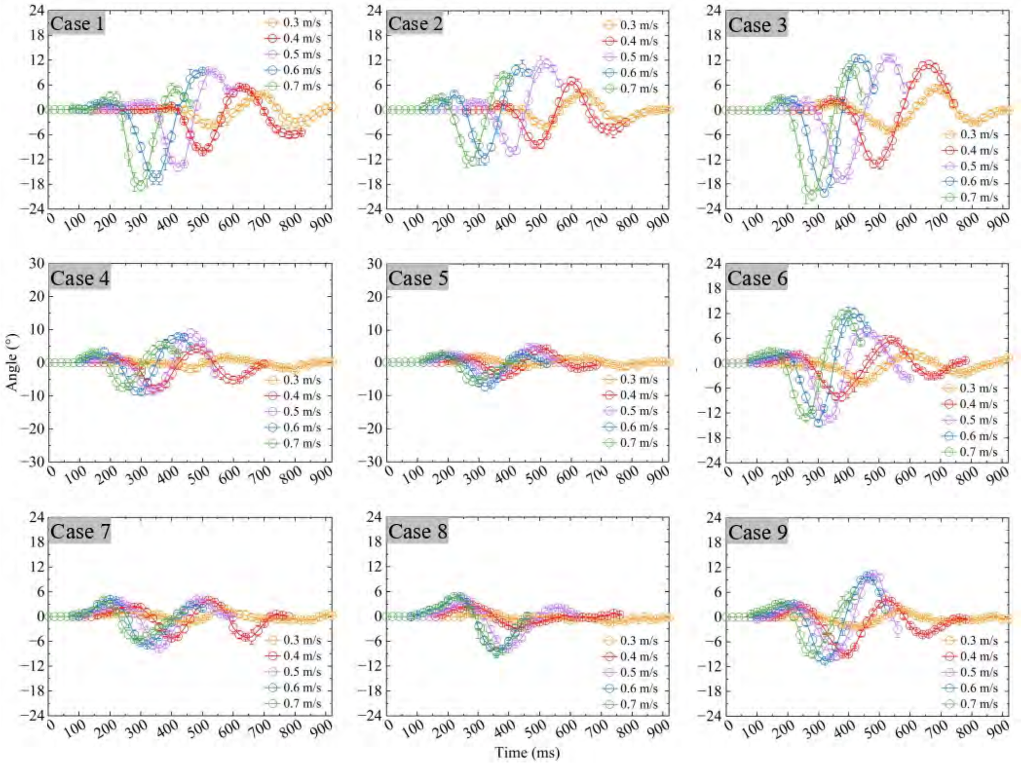

Figure 31. The variation of the tilt angle α_T of small ice floes over time. The results were obtained by averaging 10 independent measurements, with error bars representing the standard deviation of the statistical results. The tilt angle becomes negative as it tilts downward from the horizontal towards the wave trough.

to the tilt angle α_T before the ice floe fractures. Using the tilt angle of Case 3 at +40 ms in figure 30(a) as a reference, $\alpha_T \approx -2°$. I_z is the moment of inertia of the cross-section of the ice floe model, which is simplified as a rectangular section with a width of 40 mm and a height of 10 mm (data referenced from figure 4(a). The flexural strength of the ice floe model is $\sigma_f = 19.80$ kPa. Setting $\sigma_b = \sigma_f$, the fracture length can be calculated as $x \approx 86.6$ mm, which is approximately equal to the length of 5 ice floe units. This is close to the number of sub-floes ahead of the crack observed in figure 30(e). The self-weight of the overhanging portion of the ice floe model can generate sufficient bending moment to cause fracture. Considering that manual errors may be introduced during the ice floe preparation process, the fracture location may vary.

Figure 31 shows the tilt angle curves of small ice floes. After the ice floe is broken into smaller pieces, its moment of inertia decreases, making it easier to adhere to and overturn along the deformed water surface. The resulting tilt is significantly greater than that of the intact large ice floe, with the maximum tilt angle being essentially consistent with the slope angle of the depression wave. Cases 3 and 5 still induced the maximum and minimum floe tilting, respectively. For Case 3, the tilt angle reached −20.7° at a towing speed of 0.7 ms^{-1} (wave slope angle approximately −22.4°). For Case 5, the maximum tilt angle occurred at 0.6 ms^{-1}, reaching −7.3° (wave slope angle approximately −7.8°). It was also found that the convex wave more easily caused tilting of small ice floes. Compared to the large ice floe, upward tilting induced by the convex wave occurred in most cases for small floes, possibly due to their lower inertia. Cases 3, 6, and 9 still produced the most

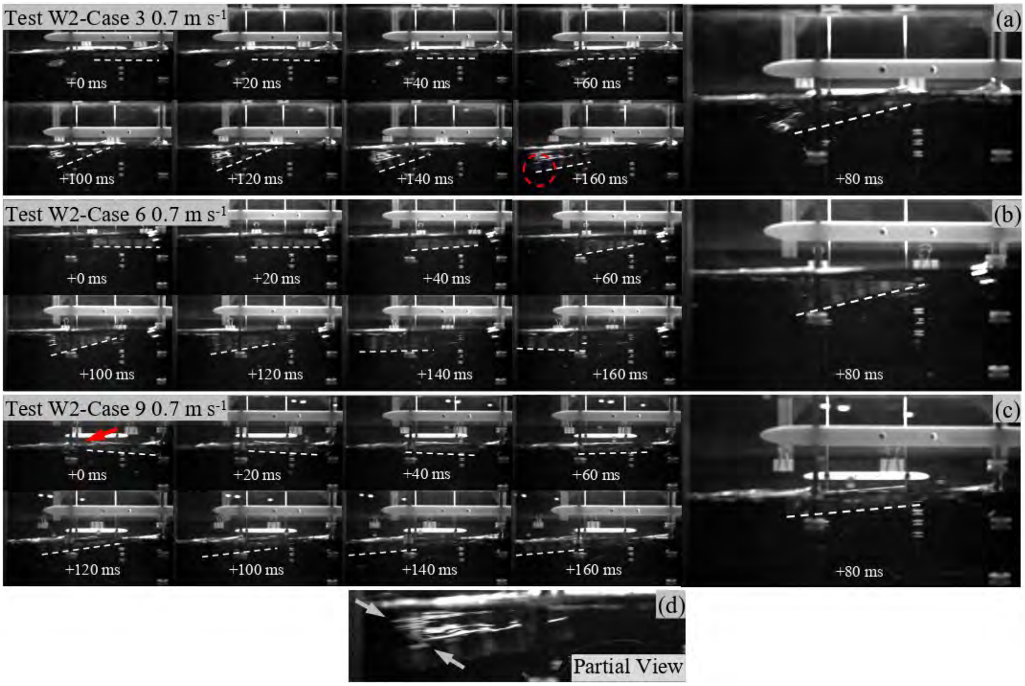

Figure 32. Tilting effect of depression waves on the small ice floe model at maximum towing speed. The figure presents a snapshot of one selected set of experimental results. Subfigure (a), (b), and (c) correspond to Cases 3, 6, and 9, respectively. The dashed lines in the images indicate the inclined state of the ice floe model in each frame. (d) A partial view of the area marked by the red-dashed circle in subfigure (a), with gray arrows indicating waves washing over the floating ice.

pronounced floe tilting. Figure 32 records their sequential snapshots as they swim beneath the ice floe at the maximum towing speed; typically, the maximum tilt angle is reached between +80 ms and +100 ms in the figures. In Case 9, it can be seen that the convex wave lifts the floe, which then collides with the convex wave. Subsequently, the convex wave is suppressed until the floe slides into the wave trough, after which the convex wave recovers (see +140 ms to +160 ms). Due to the smaller size of the floe, its potential energy is converted into kinetic energy as it slides down the depression wave. The leading edge of the floe submerges into the upward slope on the downstream side of the wave trough, and the following wave crest then submerges the upper surface of the floe. This moment is captured in the +160 ms subplot of figure 32(a), with a detailed local view shown in figure 32(d). The area between the grey arrows indicates the upward slope downstream of the wave trough. This phenomenon is entirely consistent with documented footage of orcas using waves to wash seals off ice floes. Considering that the inertia of real ice floes is much greater than that of the models used in this experiment, the actual wave-washing effect in nature is likely more pronounced. The tail-generated depression waves produced by cooperating orca groups can first be used to break up large ice floes, and subsequently to wash seals off smaller ice floes.

3.4. *The effect of depression wave on the forces acting on an ice floe unit.*

Killer whales adjust their ice-breaking strategies based on the surrounding ice conditions when hunting seals. When numerous ice fragments are present, they collaborate to push the seal-bearing floe to open water using their heads before forming a line to generate

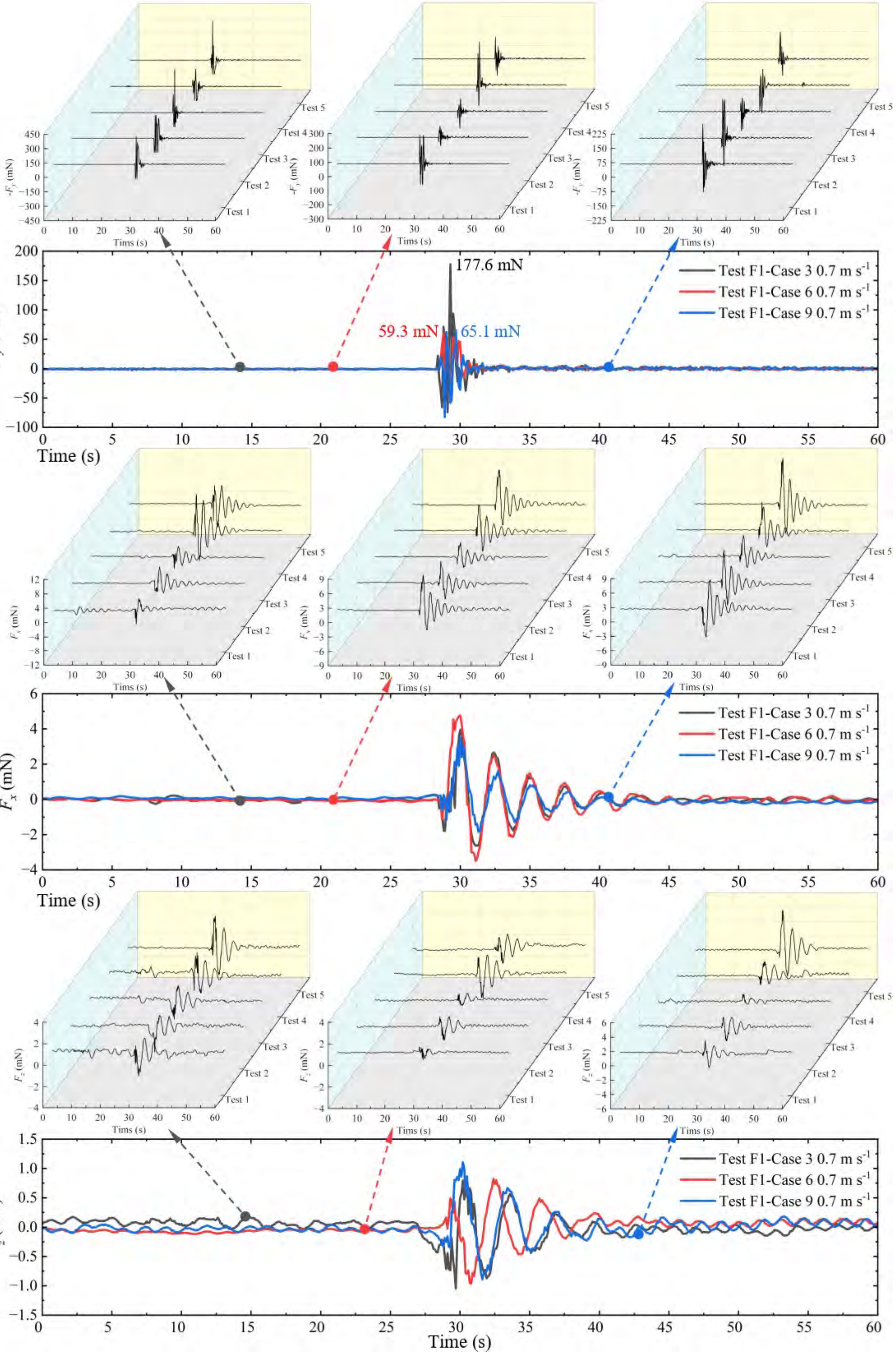

Figure 33. The effect of depression waves on the normal (y-axis), streamwise (y-axis), and spanwise (y-axis) force components acting on the single ice floe unit for Cases 3, 6, and 9 at a towing speed of 0.7 ms^{-1}.

waves for hunting. To validate the rationale behind this behavior, we designed a set of micro-force measurement experiments to assess the influence of depression waves on ice floe units. In Test F1, the ice floe unit model was set up without any obstruction between it and the killer whale model. In Test F2, a large, continuous ice floe was placed upstream of the target ice floe unit to evaluate its effect on the force response of the downstream unit. In Test F3, discrete large ice floes were arranged upstream to assess the impact of fragmented ice fields on the force experienced by the downstream floe unit. The experimental setup is illustrated in figure 4.

In Section 3.3, only Case 3 achieved 'ice breaking' at the maximum towing speed. To compare the effects of stern waves with different depression depths on the force responses of ice floe units, representative Cases 3, 6, and 9 were selected for investigation at the maximum towing speed. Each case was tested five times independently (see the 5 curves in the sub-figures), and the average of the results was taken. Figure 33 shows the time-varying three-dimensional forces measured by the force balance, with a time resolution of 0.1 ms.

For the spanwise force, it is observed that $F_z \sim O\left(10^{-1}\right)$ mN. Considering the symmetry of the floe's environment, the effect of the depression wave in the spanwise direction is extremely limited. The streamwise force increases significantly, with $F_x \sim O\left(10^{0}\right)$ mN. The amplitude and phase of F_x are essentially consistent among the three cases, reaching a maximum of about 4.0 mN. Hence, the streamwise force on the ice floe unit is largely unaffected by the geometric dimensions of the depression wave.

In contrast, the normal force differs substantially. For Case 3, the maximum normal force reaches 177.6 mN, with a peak duration < 0.2 ms whereas for Cases 6 and 9 the values are only 59.3 mN and 65.1 mN, respectively. The corresponding depression-wave depths for the three cases are 22.8 mm, 10.0 mm, and 7.8 mm. A deeper depression wave appears to induce a larger peak normal force. Notably, the gravity of the ice floe unit is only about 22.9 mN, so the maximum downward force generated by the wave is 7.8 times the floe's weight. This indicates that, in addition to gravity, other forces contribute significantly over a limited time during the floe's capsizing into the depression wave. These forces may include the viscous force induced by the descending liquid surface along the floe wall and the pressure-difference force caused by the pressure difference between the upper and lower surfaces of the floe. However, their contributions to moment generation are likely limited, as both depend on the relative position and motion state of the solid-liquid two-phase system. Saddier *et al.* (2024) studied the fragmentation of particle rafts (composed of tens-of-micron particles) under wave action and pointed out that the breakup is mainly caused by viscous forces associated with surface waves. Although the fracture patterns resemble those of ice floe break-up, viscous forces are negligible for real-world sea-ice scenarios, where ice fracture is primarily driven by bending stresses.

Figure 34 shows the effect of a large ice floe in front of the measurement point on the results. The spanwise force remains at a relatively low level, $F_z \sim O\left(10^{-1}\right)$ mN, with no significant differences in amplitude or phase. In contrast, when a large, continuous ice floe is present upstream of the measurement point, the second peak of the streamwise force F_x increases sharply, rising by approximately 3.3 times. This is likely due to resonant interaction between the subsequent oscillations of the large ice floe and the measurement point (Li *et al.* 2024), where vibrations from the large floe are transmitted through the water surface to the ice floe unit (experimental observations showed that after the depression wave passed, the large floe drifted downstream, reducing the distance between them). The amplitude of the first peak of F_x(3.5 mN) is essentially consistent with the result obtained without a large continuous floe (4.0 mN), although a slight phase shift is observed, possibly related to the reduced speed of the depression wave as it interacts with the large ice floe. For the discrete large ice floe configuration, no significant change in the amplitude of

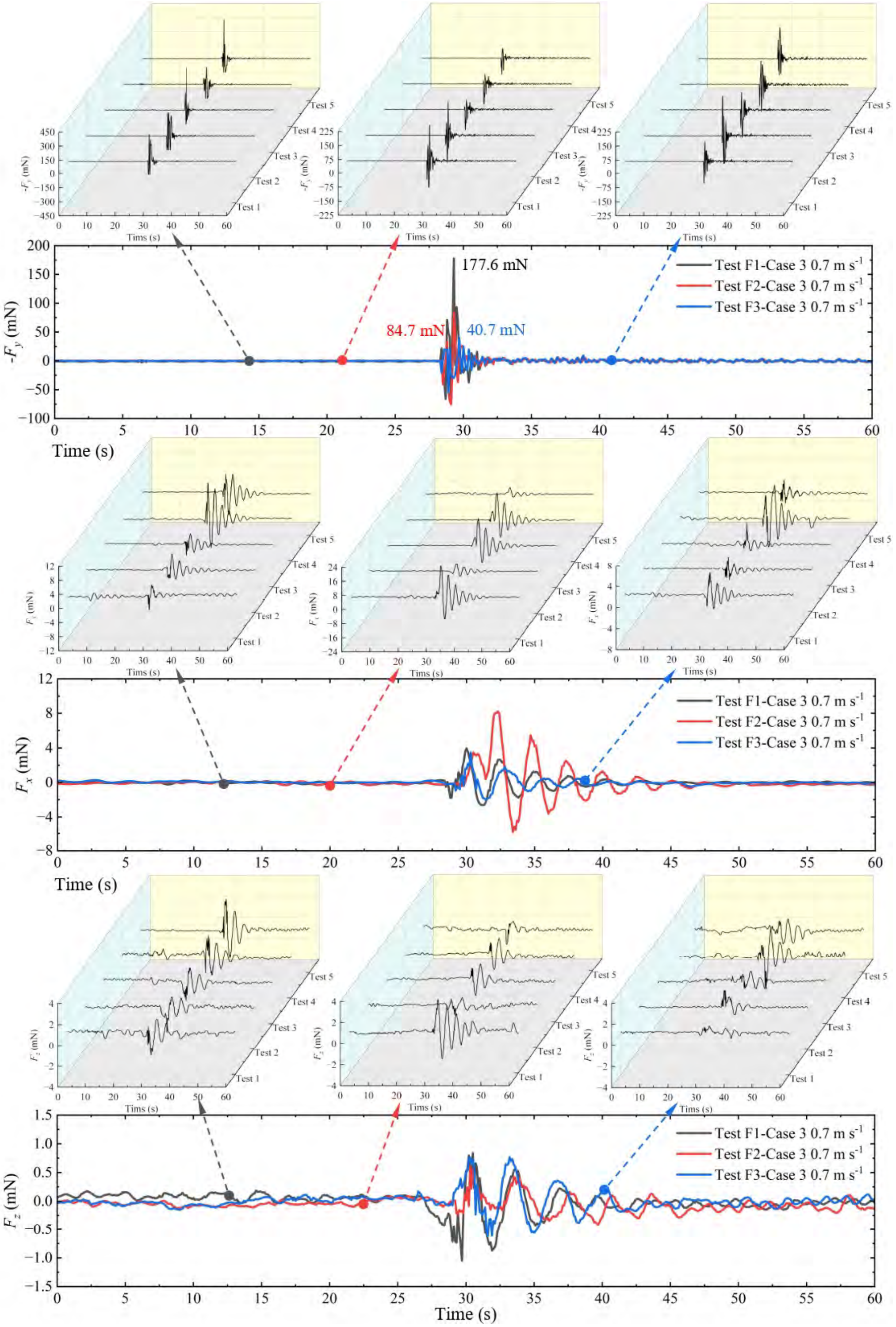

Figure 34. The effects of the depression wave on the normal (y-axis), streamwise (y-axis), and spanwise (y-axis) force components acting on a single ice floe unit; a single ice floe unit downstream of a large continuous ice floe; and a single ice floe unit downstream of a large discrete ice floe, for Case 3 at a towing speed of 0.7 ms^{-1}.

the streamwise force is observed, only a minor phase delay. Before a brittle fracture, a continuous ice floe can be considered a rigid body with high inertia. When the wavelength of the depression wave is smaller than the floe length, it generally cannot induce large tilting or oscillations in the floe; however, the subsequent vibrations of the floe can still disturb the surrounding waves. In contrast, the sub-units of a discrete ice floe tend to distribute and conform to the curved water surface individually, rather than vibrating as a single entity. Collisions between surrounding small ice floes and viscous damping in the water dissipate energy more effectively (Guyenne & Părău 2017). As shown in the normal-force results in figure 34, the attenuation of the normal force is more pronounced behind the discrete large ice floe, where the measured peak normal force is only 40.7 mN. Behind the continuous large ice floe, the peak normal force is 84.7 mN. Both values are significantly lower than the peak normal force (117.6 mN) measured on an isolated ice floe unit in open water. Clearly, when the target is located in unobstructed open water, the depression wave can produce the most significant normal force, thereby generating sufficient bending moment for ice breaking. Finally, it should be noted that the experiments in this section also have limitations. First, the experiments cannot simulate the overturning process of large ice floes, nor can they capture the contribution of various force components to the bending stress during tilting. Monitoring the dynamic parameters of large-scale simulated or real ice floes presents a significant challenge. Second, the ice floe unit is rigidly connected to the force balance carbon rod during measurement, which differs from the actual floating state of ice on the water surface. This discrepancy may introduce errors in the results.

4. Conclusion

In this paper, we investigate a compelling topic: how orcas capture seals resting on ice floes. We observed that when a pod of orcas approaches an ice floe, they consistently raise their heads, tilt their bodies upward, and slap their caudal fins downward against the water, thereby generating a pronounced stern depression wave. They utilize this wave to break up ice or wash over the surface of the floe, ultimately driving the seals into the water to complete the hunt. Through towing tank experiments, this study examines the hydrodynamics of a complex biomimetic orca pod model near a free surface, aiming to explore how variations in body and caudal fin posture influence wake structures and free-surface depression waves. We systematically investigated the wake and interfacial regimes across a posture matrix defined by three body inclination angles (10°/0°/−10°) and three caudal fin angles (30°/0°/−30°) at towing speeds ranging from 0.3 to 0.7 m s^{-1}. The aforementioned findings were validated and analyzed in detail.

In most of our experimental cases, a jet flow can be observed between the model and the free surface. Due to the Coandă effect, the jet attaches to the model surface, and adjusting the posture can modify the attachment length of the jet and the development direction of the wake. For Case 3 (body angle 10°, caudal fin angle −30°), at the maximum towing speed, the jet successively attaches to both the model surface and the deformed depression wave surface, forming a continuous channel. The downward-directed jet pulls the free surface, causing larger surface deformation. The energy of the jet sustains interfacial stability and directs trailing vortices away from the free surface. As a result, the depression wave maintains a low potential energy state, making it available for subsequent ice-breaking and wave-washing processes.

Four distinct wake regimes downstream of the orca pod model have been identified. At low Reynolds numbers and shallow depression depths, capillary waves emerge downstream of the depression wave, inducing localized vorticity aggregation near the trough. The diffusing fine-scale vortex structures interact weakly with the free surface over a limited region, gradually attenuating or disappearing as they develop downstream. As the Reynolds number increases and the depression deepens, the interface and trough become sharpened, and intense flow separation occurs at the trough bottom. This results in a large area of densely broken vortex structures downstream, diffusing substantial surface vorticity downward into the water. With a further increase in Reynolds number, the jet above the model attaches to the free surface, leading to the disappearance of capillary waves. The interface downstream may then exhibit either large-scale vortex-induced disturbances or a smooth free surface, depending on the strength of the jet and the trajectory, intensity, and extent of the shed large-scale vortex structures. When the jet propagates toward deeper water, it carries trailing vortices away from the free surface, isolating energy exchange between them, thereby promoting the formation of a smooth interface. Conversely, if the thickness or intensity of the trailing vortices is significant and the jet is weakened such that effective isolation cannot be established, the interface is perturbed by large-scale structures, leading to periodic undulations. The degree of free-surface deformation induced by a complex bluff body cannot be simply assessed by the Froude number alone, as the influence of bluff-body disturbance on free-surface shape may be comparable to that of Froude-number effects.

Experiments on the coupled interaction between ice floes and moving depression waves demonstrate that for large ice floes, the moving depression wave first induces tilting on the outer side of the floe. When the tilting speed of the floe lags behind the propagation speed of the depression wave, a cantilever state forms at the floe edge. Once the bending stress exceeds the internal strength of the ice, fracture occurs. Smaller ice floes, by contrast, adhere to the curved surface of the depression wave and undergo large-angle overturning. The upslope surface downstream of the trough then washes over the upper surface of the sliding floe, producing a wave-washing effect, which aligns with existing observational records of orca ice-breaking. Force-measurement experiments reveal that the instantaneous force exerted on the ice floe unit as the depression wave passes is significantly greater than the floe's own weight. It is inferred that viscous and pressure-difference forces induced by relative motion also contribute to the normal force. When the ice floe unit is surrounded by either a continuous large ice sheet or discrete ice fragments, the peak normal-force response decreases sharply, indicating that surrounding ice dissipates wave energy. This explains why orcas tend to perform wave-generation hunting in clean, ice-free waters.

This paper proposes that flow-jet control can be achieved by modifying the shape and posture of underwater objects or submersibles, thereby enabling active intervention in wake development patterns, interface geometry, and interface flow regimes. This approach holds significant implications for extending research on bluff-body hydrodynamics beneath a free surface.

Acknowledgements

All authors sincerely thank the anonymous reviewers for carefully reviewing this manuscript and their insightful comments and suggestions.

Funding

The authors acknowledge financial support from the China Scholarship Council (Grant No. 202406290246); the National Key Research and Development Program of China (Grant No. 2024YFB3408800); and the National Natural Science Foundation of China (Grant No. 52475607).

Declaration of interests

The authors have no conflicts to disclose.

Data availability statement

Data will be made available on request.

Declaration of generative AI in scientific writing

AI and AI-assisted technologies have only been used in the writing process to improve the readability and language of the manuscript. After using this tool, the authors reviewed and edited the content as needed and take full responsibility for the content of the published article.

Author ORCIDs

Wenyuan Zhou, https://orcid.org/0000-0003-2207-4652;
Jiale An, https://orcid.org/0009-0005-2852-0774;
Lamberto Rondoni, https://orcid.org/0000-0002-4223-6279;
Yuliang Zhang, https://orcid.org/0009-0000-7009-6130;
Zhaoyang Ou, https://orcid.org/0000-0002-4871-3515;
Yang He, https://orcid.org/0000-0003-4659-9349;
Weizheng Yuan, https://orcid.org/0000-0001-9490-7188.

Author contributions

Wenyuan Zhou-Conceptualization, Writing-Original Draft, Writing - Review & Editing, Formal Analysis, Methodology, Validation, Software, Investigation, Resources, Data Curation, Visualization, Funding Acquisition, Project Administration, Supervision. **Jiale An**-Formal Analysis, Validation, Investigation, Visualization. **Lamberto Rondoni**-Formal Analysis, Investigation. **Yuliang Zhang**-Investigation. **Zhaoyang Ou**-Investigation. **Yang He**-Funding Acquisition. **Weizheng Yuan**-Funding Acquisition.

REFERENCES

ACKLEY, S.F., BENGTSON, J.L., BOVENG, P., CASTELLINI, M., DALY, K.L., JACOBS, S., KOOYMAN, G.L., LAAKE, J., QUETIN, L., ROSS, R. & ET AL. 2003 A top-down, multidisciplinary study of the structure and function of the pack-ice ecosystem in the eastern ross sea, antarctica. *Polar Record* **39** (3), 219–230.

AHMED, N. A. 2019 *Coanda Effect: Flow Phenomenon and Applications*. Boca Raton: CRC Press.

ALZABARI, FAWAZ 2025 Hydrodynamics of a single cylinder in free-surface flow. *AIP Advances* **15** (5), 055315.

ALZABARI, FAWAZ, WILSON, CATHERINE A.M.E. & OURO, PABLO 2023 Unsteady vortex shedding dynamics behind a circular cylinder in very shallow free-surface flows. *Computers & Fluids* **260**, 105918.

BAIRD, ROBIN W. & DILL, LAWRENCE M. 1996 Ecological and social determinants of group size in transient killer whales. *Behavioral Ecology* **7** (4), 408–416.

BARKER, STEVEN J. & CROW, STEVEN C. 1977 The motion of two-dimensional vortex pairs in a ground effect. *Journal of Fluid Mechanics* **82** (4), 659–671.

BESTER, MARTHÁN N., BORNEMANN, HORST & MCINTYRE, TREVOR 2017 *Antarctic marine mammals and sea ice*, chap. 22, pp. 534–555. John Wiley & Sons, Ltd.

BLANC, MILLAT & MARTÍNEZ-RINCÓN, RAÚL O. 2023 Global scale study of the environmental preferences and distribution of orcinus orca. *Journal of Coastal Conservation* **27** (6), 60.

BOUSCASSE, BENJAMIN, COLAGROSSI, ANDREA, MARRONE, SALVATORE & SOUTO-IGLESIAS, ANTONIO 2017 Sph modelling of viscous flow past a circular cylinder interacting with a free surface. *Computers & Fluids* **146**, 190–212.

BOUTIN, GUILLAUME, ARDHUIN, FABRICE, DUMONT, DANY, SÉVIGNY, CAROLINE, GIRARD-ARDHUIN, FANNY & ACCENSI, MICKAEL 2018 Floe size effect on wave-ice interactions: Possible effects, implementation in wave model, and evaluation. *Journal of Geophysical Research: Oceans* **123** (7), 4779–4805.

BRØNS, M., THOMPSON, M. C., LEWEKE, T. & HOURIGAN, K. 2014 Vorticity generation and conservation for two-dimensional interfaces and boundaries. *Journal of Fluid Mechanics* **758**, 63–93.

BUKATOV, A. E. & ZHARKOV, VOLODYMYR 1995 Influence of a floating elastic plate on the surfaceeffects of internal waves generated by motion of a source in a non-homogeneous liquid. *Fluid Dynamics* **30**, 254–260.

CARBERRY, JOSIE 2002 Wake states of a submerged oscillating cylinder and of a cylinder beneath a free-surface,. PhD thesis, Monash University,.

CHEN, TONG & CHWANG, ALLEN T. 2002 Trailing vortices in a free-surface flow. *Physics of Fluids* **14** (2), 827–838.

CLEAVER, DAVID J., CALDERON, DARIO E, WANG, ZHIJIN & GURSUL, ISMET 2013 Periodically plunging foil near a free surface. *Experiments in Fluids* **54**, 1–18.

DAICHIN & LEE, SANGJOON 2004 Near-wake flow structure of elliptic cylinders close to a free surface: Effect of cylinder aspect ratio. *Experiments in Fluids* **36**, 748–758.

DAS, DILIP & MANDAL, B.N. 2010 Wave radiation by a sphere submerged in a two-layer ocean with an ice-cover. *Applied Ocean Research* **32** (3), 358–366.

DEIKE, LUC, POPINET, STEPHANE & MELVILLE, W. KENDALL 2015 Capillary effects on wave breaking. *Journal of Fluid Mechanics* **769**, 541–569.

Dimas, Athanassios A. & Triantafyllou, George S. 1994 Nonlinear interaction of shear flow with a free surface. *Journal of Fluid Mechanics* **260**, 211–246.

Dumont, D., Kohout, A. & Bertino, L. 2011 A wave-based model for the marginal ice zone including a floe breaking parameterization. *Journal of Geophysical Research: Oceans* **116** (C04001).

Duncan, James H. & Dimas, Athanassios A. 1996 Surface ripples due to steady breaking waves. *Journal of Fluid Mechanics* **329**, 309–339.

Duncan, J. H., Philomin, V., Behres, M. & Kimmel, J. 1994 The formation of spilling breaking water waves. *Physics of Fluids* **6** (8), 2558–2560.

Duncan, James H., Qiao, Haibing, Philomin, Vasanth & Wenz, Alexandra 1999 Gentle spilling breakers: crest profile evolution. *Journal of Fluid Mechanics* **379**, 191–222.

Fage, Arthur & Johansen, F. C. 1927 On the flow of air behind an inclined flat plate of infinite span. *Proceedings of the Royal Society of London. Series A, Containing Papers of a Mathematical and Physical Character* **116** (773), 170–197.

Fish, Frank E. 1998 Comparative kinematics and hydrodynamics of odontocete cetaceans: Morphological and ecological correlates with swimming performance. *Journal of Experimental Biology* **201** (20), 2867–2877.

Fransson, Lennart 2002 Seasonal effects on the flexural strength of river ice. In *Proceedings of the 16th IAHR International Symposium on Ice*, pp. 24–31. New York, USA.

Gomit, Guillaume, Chatellier, Ludovic & David, Laurent 2022 Free-surface flow measurements by non-intrusive methods: a survey. *Experiments in Fluids* **63**.

Guinet, Christophe, Domenici, Paolo, Stephanis, Renaud, Ford, John & Verborgh, Philippe 2007 Killer whale predation on bluefin tuna: Exploring the hypothesis of the endurance-exhaustion technique. *Marine Ecology Progress Series* **347**, 111–119.

Guo, Chunyu, Ji, Minglei, Han, Yang, Liu, Tian, Wu, Yanyuan & Kuai, Yunfei 2023 Numerical simulation of the horizontal rotating cylinder and the air entrainment near the free surface. *Physics of Fluids* **35** (9), 092115.

Guyenne, Philippe & Părău, Emilian I. 2017 Numerical study of solitary wave attenuation in a fragmented ice sheet. *Phys. Rev. Fluids* **2**, 034002.

Haller, G. 2005 An objective definition of a vortex. *Journal of Fluid Mechanics* **525**, 1–26.

Han, Hongwei, Jia, Qing, Huang, Wenfeng & Li, Zhijun 2016 Flexural strength and effective modulus of large columnar-grained freshwater ice. *Journal of Cold Regions Engineering* **30** (2), 04015005.

Hoyt, J. & Sellin, R. 2000 A comparison of tracer and piv results in visualizing water flow around a cylinder close to the free surface. *Experiments in Fluids* **28**, 261–265.

Iafrati, A. & Campana, E. F. 2005 Free-surface fluctuations behind microbreakers: space-time behaviour and subsurface flow field. *Journal of Fluid Mechanics* **529**, 311–347.

Inoue, Osamu & Sakuragi, Akira 2008 Vortex shedding from a circular cylinder of finite length at low reynolds numbers. *Physics of Fluids* **20** (3), 033601.

Jefferson, Thomas A., Stacey, Pam J. & Baird, Robin W. 1991 A review of killer whale interactions with other marine mammals: predation to co-existence. *Mammal Review* **21** (4), 151–180.

Jin, Qiu, Hudson, Dominic, Temarel, Pandeli & Price, W. Geraint 2021 Turbulence and energy dissipation mechanisms in steady spilling breaking waves induced by a shallowly submerged hydrofoil. *Ocean Engineering* **229**, 108976.

Karmakar, Avijit & Saha, Arun K. 2020 Unsteady flow past a square cylinder placed close to a free surface. *Physics of Fluids* **32** (12), 123610.

Kheisin, D. E. 1967 *Dynamics of the ice cover*. Leningrad: Gidrometeoizdat.

Kozin, V.M. & Zemlyak, V.LInfluence of Ice Cover on the Motion of a Submerged Body. 2012 Study on wave resistance of a submarine moving under an ice sheet. In *Proceedings of the Twenty-fourth (2014) International Ocean and Polar Engineering Conference*.

Kozin, V. M. & Onishchuk, A. V. 1994 Model investigations of wave formation in solid ice cover from the motion of a submarine. *Journal of Applied Mechanics and Technical Physics* **35** (2), 235–238.

Kozin, Victor M. & Pogorelova, Alexandra V. 2008 Submarine moving close to ice surface conditions. *International Journal of Offshore and Polar Engineering* **18** (04).

Li, Zhifu, Shi, Yuyun & Wu, Guoxiong 2017 Large amplitude motions of a submerged circular cylinder in water with an ice cover. *European Journal of Mechanics - B/Fluids* **65**, 141–159.

Li, Z. F., Shi, Y. Y., Shao, F. & Ning, D. Z. 2024 Wave interaction with a floating finite elastic plate of arbitrary shape. *Phys. Rev. Fluids* **9**, 094805.

Lin, J. C. & Rockwell, D. 1995 Evolution of a quasi-steady breaking wave. *Journal of Fluid Mechanics* **302**, 29–44.

Lin, J.-C., Towfighi, J. & Rockwell, D. 1995 Instantaneous structure of the near-wake of a circular cylinder: on the effect of reynolds number. *Journal of Fluids and Structures* **9** (4), 409–418.

Longo, Sandro, Chiapponi, Luca & Clavero, María 2014 Experimental analysis of the coherent structures and turbulence past a hydrofoil in stalling condition beneath a waterâĂŞair interface. *European Journal of Mechanics - B/Fluids* **43**, 172–182.

Longuet-Higgins, Michael S. 1992 Capillary rollers and bores. *Journal of Fluid Mechanics* **240**, 659–679.

Lu, Dongqiang & Dai, Shiqiang 2008 Flexural- and capillary-gravity waves due to fundamental singularities in an inviscid fluid of finite depth. *International Journal of Engineering Science* **46** (11), 1183–1193.

Lugt, Hans J. 1987 Local flow properties at a viscous free surface. *The Physics of Fluids* **30** (12), 3647–3652.

Lugt, Hans J. & Ohring, Samuel 1992 The oblique ascent of a viscous vortex pair toward a free surface. *Journal of Fluid Mechanics* **236**, 461–476.

Mellor, Malcolm 1986 *Mechanical Behavior of Sea Ice*, pp. 165–281. Boston, MA: Springer US.

Montiel, F. & Squire, V. A. 2017 Modelling wave-induced sea ice break-up in the marginal ice zone. *Proceedings of the Royal Society A: Mathematical, Physical and Engineering Sciences* **473** (2206), 20170258.

Nakamura, Yasuharu, Ohya, Yuji & Tsuruta, Hideki 1991 Experiments on vortex shedding from flat plates with square leading and trailing edges. *Journal of Fluid Mechanics* **222**, 437–447.

Ni, Baoyu, Xiong, Hang, Han, Duanfeng, Sun, Linhua, Tan, Hao & Zeng, Lingdong 2024*a* A review of ice deformation and breaking under flexural-gravity waves induced by moving loads. *Journal of Marine Science and Application* **24**, 1–18.

Ni, Bao Yu, Han, Duan Feng, Di, Shao Cheng & Xue, Yan Zhuo 2020 On the development of ice-water-structure interaction. *Journal of Hydrodynamics* **32** (4), 629–652.

Ni, B.-Y., Semenov, Y.A., Khabakhpasheva, T.I., Părău, E.I. & Korobkin, A.A. 2024*b* Nonlinear ice sheet/liquid interaction in a channel with an obstruction. *Journal of Fluid Mechanics* **983**, A41.

Ohring, Samuel & Lugt, Hans J. 1991 Interaction of a viscous vortex pair with a free surface. *Journal of Fluid Mechanics* **227**, 47–70.

Orellana-Vásquez, Hernán, Echeverría, Galo, Moscoso, Jacob, Díaz-Pazmiño, Santiago & Alarcón-Ruales, Daniela 2025 Killer whale (*Orcinus orca*) opportunistic predation events on whale sharks (*Rhincodon typus*) in the eastern tropical pacific. *Marine Mammal Science* p. 0:e70007.

Pancaldi, Francesca, Ayres, Kathryn A., Gallagher, Austin J., Moskito, James, Williamson, Kelsey C. & Higuera Rivas, Jesús Erick 2024 Killer whales (orcinus orca) hunt, kill and consume the largest fish on earth, the whale shark (rhincodon typus). *Frontiers in Marine Science* **11**.

Patel, Kuntal, Sun, Jun, Yang, Zixuan & Zhu, Xiaojue 2025 Coupled liquid-gas flow over a submerged cylinder: interface topology, wake structure and hydrodynamic lift. *Journal of Fluid Mechanics* **1008**, A10.

Perry, A. E. & Steiner, T. R. 1987 Large-scale vortex structures in turbulent wakes behind bluff bodies. part 1. vortex formation processes. *Journal of Fluid Mechanics* **174**, 233–270.

Petrich, Chris & Eicken, Hajo 2009 *Growth, Structure and Properties of Sea Ice*, chap. 2, pp. 23–77. John Wiley & Sons, Ltd.

Petrich, Chris & Eicken, Hajo 2017 *Overview of sea ice growth and properties*, chap. 1, pp. 1–41. John Wiley & Sons, Ltd.

Pitman, Robert L., Ballance, Lisa T., Mesnick, Sarah I. & Chivers, Susan J. 2001 Killer whale predation on sperm whales: observations and implications. *Marine Mammal Science* **17** (3), 494–507.

Pitman, Robert L. & Durban, John W. 2012 Cooperative hunting behavior, prey selectivity and prey handling by pack ice killer whales (orcinus orca), type b, in antarctic peninsula waters. *Marine Mammal Science* **28** (1), 16–36.

Pogorelova, A. 2011 Unsteady motion of a source in a fluid under a floating plate. *Journal of Applied Mechanics and Technical Physics* **52**, 707–726.

Pogorelova, A. & Kozin, Victor 2011 Effect of water depth on ice plate deflections for moving submarine. In *Proceedings of the Twenty-first (2011) International Offshore and Polar Engineering Conference*, pp. 1003–1007.

Pogorelova, A. & Kozin, V.M. 2014 Ice plate deflections due to a submerged source on a sloped sea bed. *Proceedings of the 11th (2014) Pacific/Asia Offshore Mechanics Symposium, PACOMS 2014* pp. 127–132.

Pogorelova, A., Zemlyak, Vitali & Kozin, Victor 2018 Moving of a submarine under an ice cover in fluid of finite depth. *Journal of Hydrodynamics* **31**, 562–569.

Pogorelova, A.V., Zemlyak, V.L. & Kozin, V.M. 2019 Body motion in liquid under ice plate with snow cover. *Applied Ocean Research* **84**, 32–37.

Pogorelova, Alexandra V. & Kozin, Victor M. 2010 Flexural-gravity waves due to unsteady motion of point source under a floating plate in fluid of finite depth. *Journal of Hydrodynamics, Ser. B* **22** (5), Supplement: 71–76.

Reichl, P., Hourigan, K. & Thompson, M. C. 2005 Flow past a cylinder close to a free surface. *Journal of Fluid Mechanics* **533**, 269–296.

Reisinger, Ryan R., Keith, Mark, Andrews, Russel D. & de Bruyn, P.J.N. 2015 Movement and diving of killer whales (orcinus orca) at a southern ocean archipelago. *Journal of Experimental Marine Biology and Ecology* **473**, 90–102.

Saddier, Louis, Palotai, Ambre, Aksil, Mathéo, Tsamados, Michel & Berhanu, Michael 2024 Breaking of a floating particle raft by water waves. *Phys. Rev. Fluids* **9**, 094302.

Samsam-Khayani, Hadi & Seyed-Aghazadeh, Banafsheh 2025 Free surface proximity effects on flow dynamics around a flat plate. *Journal of Fluid Mechanics* **1010**, A26.

Sareen, A., Zhao, J., Sheridan, J., Hourigan, K. & Thompson, M. C. 2018 Vortex-induced vibrations of a sphere close to a free surface. *Journal of Fluid Mechanics* **846**, 1023–1058.

Shen, Lian, Zhang, Xiang, Yue, Dick K. P. & Triantafyllou, George S. 1999 The surface layer for free-surface turbulent flows. *Journal of Fluid Mechanics* **386**, 167–212.

Sheridan, J., Lin, J.-C. & Rockwell, D. 1995 Metastable states of a cylinder wake adjacent to a free surface. *Physics of Fluids* **7** (9), 2099–2101.

Sheridan, J., Lin, J.-C. & Rockwell, D. 1997 Flow past a cylinder close to a free surface. *Journal of Fluid Mechanics* **330**, 1–30.

Smith, Thomas Gordon, Siniff, Donald B., Reichle, R. A. & Stone, Sheridan 1981 Coordinated behavior of killer whales, orcinus orca, hunting a crabeater seal, lobodon carcinophagus. *Canadian Journal of Zoology* **59**, 1185–1189.

Squire, Vernon A. 2011 Past, present and impendent hydroelastic challenges in the polar and subpolar seas. *Philosophical Transactions of the Royal Society A: Mathematical, Physical and Engineering Sciences* **369** (1947), 2813–2831.

Squire, Vernon A. 2020 Ocean wave interactions with sea ice: A reappraisal. *Annual Review of Fluid Mechanics* **52**, 37–60.

Squire, Vernon A., Dugan, John P., Wadhams, Peter, Rottier, Philip J. & Liu, Antony K. 1995 Of ocean waves and sea ice. *Annual Review of Fluid Mechanics* **27** (Volume 27, 1995), 115–168.

Sturova, I.V. 2012 The motion of a submerged sphere in a liquid under an ice sheet. *Journal of Applied Mathematics and Mechanics* **76** (3), 293–301.

Sturova, Izolda V. 2013 Unsteady three-dimensional sources in deep water with an elastic cover and their applications. *Journal of Fluid Mechanics* **730**, 392–418.

Subburaj, Rahul, Khandelwal, Prashant & Vengadesan, S. 2018 Numerical study of flow past an elliptic cylinder near a free surface. *Physics of Fluids* **30** (10), 103603.

Sun, Jun, Lu, Min, Patel, Kuntal, Zhu, Xiaojue & Yang, Zixuan 2025 Free-surface flow past a submerged horizontal cylinder: Reynolds-number dependence. *Journal of Fluid Mechanics* **1023**, A39.

Taira, Kunihiko & Colonius, Tim 2009 Three-dimensional flows around low-aspect-ratio flat-plate wings at low reynolds numbers. *Journal of Fluid Mechanics* **623**, 187–207.

Taneda, Sadatoshi 1965 Experimental investigation of vortex streets. *Journal of the Physical Society of Japan* **20** (9), 1714–1721.

Terrington, S.J., Hourigan, K. & Thompson, M.C. 2022 Vortex ring connection to a free surface. *Journal of Fluid Mechanics* **944**.

Timco, G.W. & O.'Brien, S. 1994 Flexural strength equation for sea ice. *Cold Regions Science and Technology* **22** (3), 285–298.

Timco, G.W. & Weeks, W.F. 2010 A review of the engineering properties of sea ice. *Cold Regions Science and Technology* **60** (2), 107–129.

Triantafyllou, George S. & Dimas, Athanassios A. 1989 Interaction of two-dimensional separated flows with a free surface at low froude numbers. *Physics of Fluids A: Fluid Dynamics* **1** (11), 1813–1821.

Tryggvason, Gretar, Unverdi, Salih, Song, Museok & Abdollahi-Alibeik, Javad 1991 Interaction of vortices with a free surface and density interfaces. *Vortex Dynamics and Vortex Methods* **28**.

Visser, Ingrid N., Smith, Thomas G., Bullock, Ian D., Green, Geoffrey D., Carlsson, Olle G. L. & Imberti, Santiago 2008 Antarctic peninsula killer whales (orcinus orca) hunt seals and a penguin on floating ice. *Marine Mammal Science* **24** (1), 225–234.

Wang, Y.S. 1981 Uniaxial compression testing of arctic sea ice. In *Proceedings of the Sixth Int. Conf. POAC*, , vol. 1, pp. 346–355. Quebec City, Canada.

Xiong, Hang, Ni, Baoyu, Semenov, Yuriy & Korobkin, Alexander 2025 Inertial motion of a circular cylinder approaching obliquely an ice cover. *Scientific reports* **15** (1), 9412.

Xue, Fuduo, Jin, Weiqi, Qiu, Su & Yang, Jie 2020 Wake features of moving submerged bodies and motion state inversion of submarines. *IEEE Access* **8**, 12713–12724.

You, Hojung, Hwang, Jin Hwan & Park, Yong Sung 2019 Mechanical understanding of hunting waves generated by killer whales. *Marine Mammal Science* **35** (4), 1396–1417.

Yu, Dequan & Tryggvason, Grétar 1990 The free-surface signature of unsteady, two-dimensional vortex flows. *Journal of Fluid Mechanics* **218**, 547–572.

Zemlyak, V.L., Kozin, V.M., Chizhiumov, S.D., Baurin, N.O. & Matiushina, A.A. 2019 The influence of the bottom contour on the deformed state of the ice cover due to the motion of the submarine. *Applied Ocean Research* **87**, 204–210.

Zemlyak, V.L., Pogorelova, A. & Kozin, V.M. 2013 Influence of peculiarities of the form of a submarine vessel on the efficiency of breaking ice cover. In *Proceedings of the Twenty-third (2013) International Offshore and Polar Engineering*, pp. 1252–1258.

Zemlyak, Vitaly, Pogorelova, Alexandra & Kozin, Victor 2022 Motion of a submerged body in a near-surface water environment. *International Journal of Naval Architecture and Ocean Engineering* **14**, 100433.

Zemlyak, Vitaly, Pogorelova, Alexandra & Kozin, Victor 2023 Motion of a submerged body under a free surface and an ice cover in finite water depth conditions. *Ocean Engineering* **288**, 116161.

Zemlyak, V L, Kozin, V M & Baurin, N O 2018 Influence of peculiarities of the form of a submerged body on the parameters of generated waves in the ice motion. *IOP Conference Series: Earth and Environmental Science* **193** (1), 012024.

Zhang, Kai, Hayostek, Shelby, Amitay, Michael, He, Wei, Theofilis, Vassilios & Taira, Kunihiko 2020 On the formation of three-dimensional separated flows over wings under tip effects. *Journal of Fluid Mechanics* **895**, A9.

Zhao, Feng, Wang, Rui, Zhu, Hongbo, Cao, Yong, Bao, Yan, Zhou, Dai & Han, Zhaolong 2022 Wake dynamics and hydrodynamic forces of a circular cylinder beneath a free surface. *Ocean Engineering* **265**, 112669.

Zhao, Feng, Wang, Rui, Zhu, Hongbo, Ping, Huang, Bao, Yan, Zhou, Dai, Cao, Yong & Cui, Hongyu 2021 Large-eddy simulations of flow past a circular cylinder near a free surface. *Physics of Fluids* **33** (11), 115108.

Zhou, J., Adrian, R. J., Balachandar, S. & Kendall, T. M. 1999 Mechanisms for generating coherent packets of hairpin vortices in channel flow. *Journal of Fluid Mechanics* **387**, 353–396.

Zhou, Wenyuan, Huang, Ding, He, Yang & Yuan, Weizheng 2026 Decoupling-free wind tunnel balance for high-precision measurement of three-dimensional micro-aerodynamic forces. *Measurement* **257**, 118772.

Zhou, Wenyuan, Liu, Xiangdong, Sun, Yinglu, Lyu, Xianglian, He, Yang & Yuan, Weizheng 2025 Design and validation of an air-bearing-based micro skin-friction balance for small area samples. *Experimental Thermal and Fluid Science* **164**, 111433.